Journal of Nanomaterials

Nanosensor Technology

Guest Editors: Rakesh K. Joshi and Shekhar Bhansali

Nanosensor Technology

Journal of Nanomaterials

Nanosensor Technology

Guest Editors: Rakesh K. Joshi and Shekhar Bhansali

Contents

Hindawi Publishing Corporation
Journal of Nanomaterials
Volume 2008, Article ID 840390, 1 page
doi:10.1155/2008/840390

Editorial
Nanosensor Technology

Rakesh K. Joshi and Sekhar Bhansali

College of Engineering, University of South Florida, 4202 East Fowler Avenue, Tampa, FL 33620, USA

Correspondence should be addressed to Rakesh K. Joshi, joshi@eng.usf.edu

Received 30 December 2008; Accepted 31 December 2008

Understanding the sensing mechanism in nanodimensions is very important for developing the efficient sensors. Researchers have been putting their efforts to fabricate small and ultrasensitive single nanowire sensors. Recently, the biosensors have got lot of attention due to the biotechnological advancement in the nanotechnology. Biosensor is a device used for the detection of an analyte that combines a biological component with a physiochemical detector. The advances in nanotechnology require understanding of physics, chemistry, and biology in low dimensions. Materials in the nanostructured form can achieve high response to very small targets in practical conditions. The goal of this special issue is to provide a platform for researchers working in the field of nanosensors to discuss exciting new developments on various topics in this area. We attempted the best to get high-quality review process for all the manuscripts submitted to this issue. Only five papers were accepted for publication in this issue. The first paper by Rani et al. discusses the enhancement in ammonia sensitivity of SnO_2 thin films using high-energy Ni+ ion irradiation. Authors have described the sol-gel method for SnO_2 thin film preparation. The observed enhancement in NH_3 sensitivity has been discussed in context of ion beam generated electronic states in thin films. The second paper by Zhang et al. discusses the ambient pressure synthesis of tungsten oxide nanowires and nanoparticles on AlN substrates using the hot filament CVD techniques. They present a systematic study of sensing properties of the long nanowires. The third paper by Sun et al. discusses a proposal for the design of microgyroscope based on MEMS structures. Authors in this paper demonstrate the methods to fabricate accurate and cheaper gyroscope. The fourth paper by Weber el al. presents the fabrication and characterization of ZnO nanowire array for electrochemical sensing of glucose. The authors concluded that the nanoarray sensor is highly sensitive to glucose. The issue closes with the fifth paper by Niemann et al. on significance of nanomaterials for hydrogen energy. Authors present a review on the development of nanomaterials for hydrogen storage. They suggested that a high surface/volume is very important for energy storage in nanomaterials.

ACKNOWLEDGMENTS

We thank all the contributing authors and reviewers for their help in putting together this special issue. We also thank the Editor-in-Chief of the Journal of Nanomaterials, Dr. Michael Z. Hu, for his support and encouragement. We highly appreciate Dr. Hu's contribution to the Journal of Nanomaterials.

Rakesh K. Joshi
Sekhar Bhansali

Hindawi Publishing Corporation
Journal of Nanomaterials
Volume 2008, Article ID 395490, 4 pages
doi:10.1155/2008/395490

Research Article

Enhancement of Ammonia Sensitivity in Swift Heavy Ion Irradiated Nanocrystalline SnO_2 Thin Films

Sanju Rani,[1] Somnath C. Roy,[1] N. K. Puri,[2] M. C. Bhatnagar,[1] and D. Kanjilal[3]

[1] *Thin Film Lab, Department of Physics, Indian Institute of Technology, New Delhi 110016, India*
[2] *Department of Physics, I.T.S. Engineering College, Greater Noida, Uttar Pradesh 201308, India*
[3] *Materials Science Division, Inter-University Accelerator Centre, Aruna Asaf Ali Marg, New Delhi 110075, India*

Correspondence should be addressed to Somnath C. Roy, somnath_iitd@yahoo.com

Received 12 July 2008; Accepted 24 September 2008

Recommended by Rakesh Joshi

Swift heavy ion irradiation is an effective technique to induce changes in the microstructure and electronic energy levels of materials leading to significant modification of properties. Here we report enhancement of ammonia (NH_3) sensitivity of SnO_2 thin films subjected to high-energy Ni^+ ion irradiation. Sol-gel-derived SnO_2 thin films (100 nm thickness) were exposed to 75 MeV Ni^+ ion irradiation, and the gas response characteristics of irradiated films were studied as a function of ion fluence. The irradiated films showed *p*-type conductivity with a much higher response to NH_3 compared to other gases such as ethanol. The observed enhancement of NH_3 sensitivity is discussed in context of ion beam generated electronic states in the SnO_2 thin films.

1. INTRODUCTION

Tin oxide (SnO_2) is a material widely used for gas sensing applications because of its suitable properties such as natural off-stoichiometry, chemical and thermal stability, and ease of processing [1]. Tin oxide-based gas sensors have been successfully designed to detect a variety of toxic and hazardous gases and vapors for applications ranging from domestic leak detections to industrial process control. However, because of stricter environmental regulations and process control requirements, gas sensors with higher sensitivity and selectivity are in continuous demand; hence efforts are on to tailor the properties of sensing materials such as tin oxide to achieve better gas response properties.

Swift heavy ion irradiation, in which an energetic ion beam is allowed to pass through a material, is a very effective technique to induce changes in microstructure and electronic energy levels, and has been used to tailor properties of various metallic, semiconducting, and insulating thin films [2]. When a high-energy ion beam passes through a material, it loses its energy in two distinct pathways; namely, nuclear and electronic energy losses. The nuclear energy loss dominates at lower energies, whereas higher energy beam results in electronic excitation of the target material. By suitable control of the irradiation parameters such as energy and fluence of the ion beam, it is therefore possible to tailor various properties of the target material. Ion irradiation technique has been used to tailor the structure-property relationships in several metal oxide systems; for tin oxide, however, studies have so far been limited only to variation of microstructure in powders [3, 4], and nanocrystallization in thin film [5]. An attempt to modify the gas sensing properties of tin oxide thin films by ion irradiation had resulted only in the baseline stabilization [6].

In this work, we report on the effect of 75 MeV Ni^+ ion irradiation on gas sensing properties of sol-gel-derived SnO_2 thin films. Gas sensing experiments using ammonia and ethanol on irradiated films revealed a much greater enhancement of sensitivity for ammonia with respect to ethanol. Furthermore, in comparison to unirradiated films, the irradiated films showed *p*-type conduction. The observed enhancement of gas sensitivity and selectivity to ammonia has been discussed in context of ion beam-induced changes in the material.

2. EXPERIMENTAL

SnO_2 thin films were deposited from a solution containing 10 gm of $SnCl_4 \bullet 5H_2O$ dissolved in 80 mL of 2-propanol. Thorough mixing was ensured by refluxing the solution

with magnetic stirring arrangement for 6 hours at 80°C and then the resultant solution was left for ageing for another 6 hours. This solution was then filtered through a Whatman filter paper to obtain a clear solution free of any particulate. The final solution was coated onto Corning 7059 glass by dip coating system at speed of 10 cm/min^2 for depositing one layer of the film. Each deposited layer was dried at 200°C for 15 minutes before deposition of the next layer. Final sintering of the films was carried out at 600°C after deposition of a required number of layers to obtain a desired thickness. Thickness of the deposited films was estimated by an Ambios surface profilometer and was approximately 1000 Å. These films were irradiated at room temperature by using 75 MeV Ni^+ ions at two different fluences, namely, 1×10^{11} and 1×10^{12} ions/cm^2. During the irradiation, pressure inside experimental chamber was at 1.5×10^{-6} mbar. Structural analysis of the films was done with the help of a Philips "XPert" model glancing angle X-ray diffractometer (GAXRD) in the 2θ range of 20°–60°. Microstructural characterization was performed using Technai G20-Stwin (200 KeV) high-resolution transmission electron microscope (HRTEM). For HRTEM studies the films were ultrasonically dispersed in ethanol and taken on the carbon coated grids. Gas sensing experiments were performed with an indigenously designed gas-sensing setup attached with mass flow controllers for precise measurement of gas flows at ppm level. Change in resistance of the films was measured as a function of temperature through a computer interfaced digital multimeter (DMM).

3. RESULTS AND DISCUSSION

Figure 1 shows the glancing angle XRD patterns of unirradiated and irradiated SnO_2 thin films. All peaks in the spectra correspond to the standard rutile phase with polycrystalline structure. It is observed that, in comparison to unirradiated film, the relative intensities of all peaks increase in irradiated films. Furthermore, the intensities of XRD peaks also increase with increase in ion fluence, implying that SHI beam irradiation enhances crystallinity of the SnO_2 thin films. A careful examination of the XRD patterns further reveals that the relative intensity of (110) peak in the irradiated films increases at a faster rate as compared to the intensities of the other peaks, which implies that irradiation of Ni ions also enhances the preferred orientation of the SnO_2 thin films. Increase of crystallinity along the (110) plane plays a crucial role in enhancing gas-sensing properties of SnO_2 thin films, which is discussed later.

Figure 2 compares the HRTEM images of unirradiated and irradiated SnO_2 thin films. In the unirradiated film (Figure 2(a)), the crystallites appear randomly oriented, a characteristic feature of sol-gel-derived thin films. With the ion irradiation, however, the crystallite boundaries gradually disappear and enhancement of crystallinity is observed. At higher fluence (Figure 2(c)), the crystallites show preferred orientation along (110) planes, which confirms XRD observations reported in the last paragraph.

Gas sensing experiments performed on unirradiated SnO_2 films with 1000 ppm ammonia and ethanol gases are

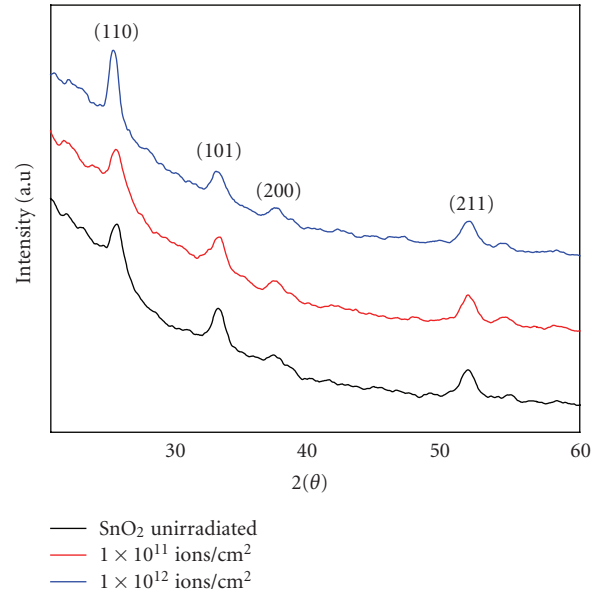

Figure 1: Glancing angle XRD patterns of unirradiated and irradiated SnO_2 thin films.

shown in Figure 3, and Figure 4 compares the responses of irradiated (with 10^{12} ions/cm^2) films under similar conditions. Here it is worth mentioning that unirradiated films show decrease of resistance when exposed to ammonia and ethanol, both reducing gases, due to normal n-type behavior; however, the irradiated films show increase of resistance under similar conditions indicating p-type conduction resulting from ion irradiation. The sensitivity factors are calculated by the equation:

$$s = ((R_g - R_a)/R_a)\%, \quad (1)$$

where R_g and R_a represent resistance in the presence of gas and air, respectively; the values of s for unirradiated and irradiated films at different temperatures are tabulated in Table 1. For the unirradiated films, the values of sensitivity "s" in ammonia and ethanol gases at 300°C are 284 and 87, respectively, while for irradiated films they increase to 516 and 115, respectively, for 1×10^{11} ions/cm^2, and to 882 and 142, respectively, for 1×10^{12} ions/cm^2. This implies that irradiation of SnO_2 thin films by high-energy ion beam, for example with a fluence of 1×10^{12} ions/cm^2, results in a 213% (284 to 882) increase in its ammonia sensitivity, while only 63% (87 to 142) increase in sensitivity for ethanol is observed under similar conditions. Such an enhancement of ammonia sensitivity can be explained in terms of the surface chemistry modifications due to ion beam irradiation.

The XRD data shown in Figure 1 shows an enhancement of crystallinity along the (110) plane resulting from Ni^+ ion irradiation, which also indicates preferred surface orientation of the irradiated SnO_2 thin films. Such a (110) surface of SnO_2 consists of two types of oxygen vacancies: the bridging oxygen vacancies created by removal of oxygen ions from the top layer of an ideal (110) surface, and the "in-plane" oxygen vacancies created by removal of oxygen

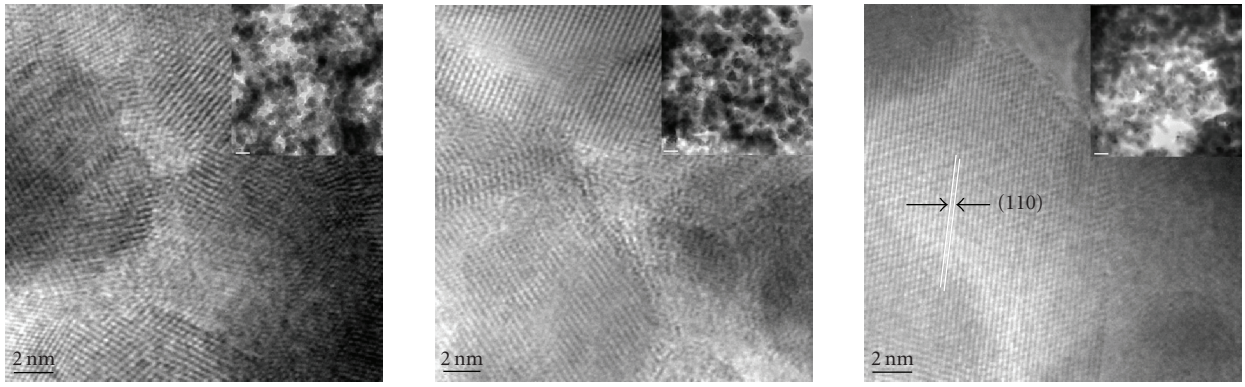

Figure 2: High-resolution TEM images of SnO_2 thin films: (a) unirradiated, (b) irradiated with 10^{11} ions/cm^2, and (c) irradiated with 10^{12} ions/cm^2.

Table 1: Sensitivity factors of unirradiated and irradiated SnO_2 thin films for ammonia and ethanol at different temperatures.

Ni^+ ion irradiation fluence	Temperature 200°C (sensitivity %)		Temperature 250°C (sensitivity %)		Temperature 300°C (sensitivity %)	
	NH_3	C_2H_5OH	NH_3	C_2H_5OH	NH_3	C_2H_5OH
Unirradiated	52	5	98	32	284	87
1×10^{11} ions/cm^2	68	15	103	53	516	115
1×10^{12} ions/cm^2	122	27	649	73	882	142

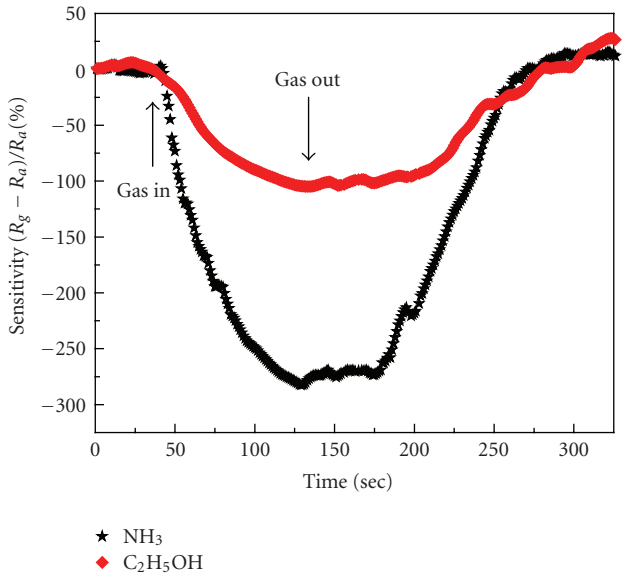

Figure 3: Gas sensing behavior of unirradiated SnO_2 thin films at 300°C, exposed to 1000 ppm ammonia (NH_3) and ethanol (C_2H_5OH) vapors.

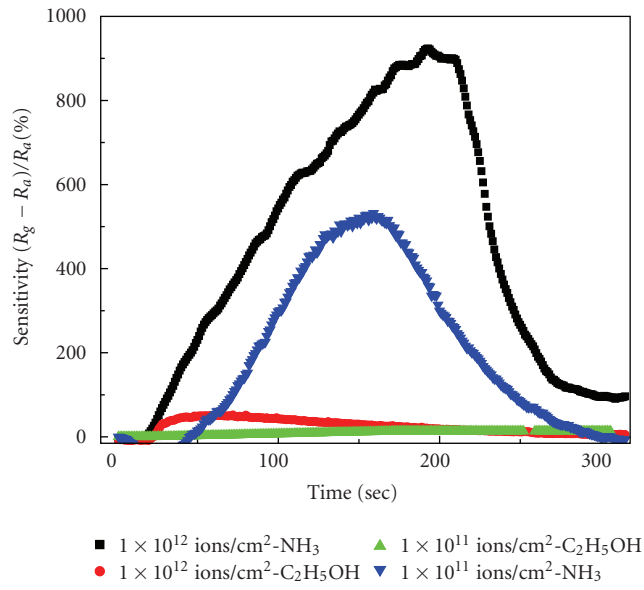

Figure 4: Gas sensing behavior of SnO_2 thin films irradiated with 1×10^{11} ions/cm^2 and 1×10^{12} ions/cm^2, exposed to 1000 ppm ammonia (NH_3) and ethanol (C_2H_5OH) vapors at 300°C.

ions from the tin containing lattice plane [7]. During the ion irradiation process, samples are kept in an ultrahigh vacuum ambience that promotes oxygen desorption, especially from the top layer resulting in the formation of "bridging" oxygen vacancies. Such oxygen vacancies may also result from the thermal spikes created in the samples during ion irradiation. The formation of bridging oxygen vacancies lowers the coordination number of the surface tin cations from an initial value of six to four, which, in turn, reduces their charge state from Sn^{4+} to Sn^{2+}. The four- coordinated Sn^{2+} ions are known to be more acidic compared to Sn^{4+} cations, which promotes a higher chemisorption of ammonia, a strongly basic gas, on the surface of the irradiated films [8]. Hence the sensitivity of high-energy ion irradiated SnO_2 thin films

toward ammonia is significantly enhanced compared to that for any other gas such as ethanol. Furthermore, the four coordinated Sn^{2+} ions create a local SnO—like environment at the surface and near surface region of the irradiated SnO_2 thin films, which results in *p*-type conductivity observed in the gas sensing experiments [9].

4. CONCLUSIONS

The present study shows that structural and gas sensing properties of SnO_2 thin films are significantly modified by 75 MeV Ni^+ ion irradiation. The crystallinity of the irradiated films is enhanced along the (110) plane that also affects the gas sensing characteristics. Gas sensing experiments with ammonia and ethanol reveal a significant enhancement of sensitivity for ammonia over ethanol that is attributed to acidic nature of the irradiated SnO_2 surfaces. Formation of bridging oxygen vacancies during the ion irradiation process converts the six coordinated Sn^{4+} cations into four coordinated Sn^{2+} cations; the latter have more acidic character than the former. This promotes a stronger chemisorption of ammonia molecules on the surface of the ion irradiated SnO_2 thin films.

ACKNOWLEDGMENT

The authors acknowledge the support of Nano Science Unit (at IIT Delhi) of NSTI, DST, Government of India for carrying out the HRTEM investigations.

REFERENCES

[1] Y. Shimizu and M. Egashira, "Basic aspects and challenges of semiconductor gas sensors," *MRS Bulletin*, vol. 24, no. 6, pp. 18–24, 1999.

[2] D. Kanjilal, "Swift heavy ion-induced modification and track formation in materials," *Current Science*, vol. 80, no. 12, pp. 1560–1566, 2001.

[3] S. Hemon, F. Gourbilleau, Ch. Dufour, E. Paumier, E. Dooryhee, and A. Rouanet, "TEM study of irradiation effects on tin oxide nanopowder," *Nuclear Instruments and Methods in Physics Research, Section B*, vol. 122, no. 3, pp. 526–529, 1997.

[4] A. Berthelot, S. Hémon, F. Gourbilleau, C. Dufour, B. Domengés, and E. Paumier, "Behaviour of a nanometric SnO_2 powder under swift heavy-ion irradiation: from sputtering to splitting," *Philosophical Magazine A*, vol. 80, no. 10, pp. 2257–2281, 2000.

[5] T. Mohanty, P. V. Satyam, and D. Kanjilal, "Synthesis of nanocrystalline tin oxide thin film by swift heavy ion irradiation," *Journal of Nanoscience and Nanotechnology*, vol. 6, no. 8, pp. 2554–2559, 2006.

[6] O. M. Merdrignac, P. T. Moseley, R. Peat, C. J. Sofield, and S. Sugden, "The modification of gas-sensing properties of semiconducting oxides by treatment with ionizing radiation," *Sensors and Actuators B*, vol. 7, no. 1–3, pp. 651–655, 1992.

[7] D. F. Cox, T. B. Fryberger, and S. Semancik, "Oxygen vacancies and defect electronic states on the $SnO_2(110)$-1×1 surface," *Physical Review B*, vol. 38, no. 3, pp. 2072–2083, 1988.

[8] M. W. Abee and D. F. Cox, "NH_3 chemisorption on stoichiometric and oxygen-deficient SnO_2 (110) surfaces," *Surface Science*, vol. 520, no. 1-2, pp. 65–77, 2002.

[9] A. Togo, F. Oba, I. Tanaka, and K. Tatsumi, "First-principles calculations of native defects in tin monoxide," *Physical Review B*, vol. 74, no. 19, Article ID 195128, 8 pages, 2006.

Hindawi Publishing Corporation
Journal of Nanomaterials
Volume 2008, Article ID 957935, 5 pages
doi:10.1155/2008/957935

Research Article

Ambient Pressure Synthesis of Nanostructured Tungsten Oxide Crystalline Films

H. X. Zhang,[1] B. Q. Yang,[1] and P. X. Feng[1, 2]

[1] *Department of Physics, University of Puerto Rico, P.O. Box 23343, San Juan, PR 00931, USA*
[2] *Department of Physics, Donghua University, Shanghai 200051, China*

Correspondence should be addressed to P. X. Feng, peterxianping@vmail.uprrp.edu

Received 5 March 2008; Accepted 28 April 2008

Recommended by Rakesh Joshi

We report the results of the ambient pressure synthesis of tungsten oxide nanowires and nanoparticles on AlN substrates using the hot filament CVD techniques. The morphologic surface, crystallographic structures, chemical compositions, and bond structures of the obtained samples have been investigated using scanning electron microscopy (SEM), X-ray diffraction (XRD), energy dispersive X-ray spectroscopy (EDX), and Raman scattering, respectively. Different morphologies were observed for different substrate temperatures, but otherwise identical growth conditions. The experimental measurements reveal the evolutions of the crystalline states and bond structures following the substrate temperatures. Besides, different substrate materials also affected the tungsten oxide nanostructures. Bundles of wire-type tungsten oxide nanowires with a length of up to 5 mm were obtained on Al_2O_3 substrate. Furthermore, the sensitive properties of the super long nanowires to the gas and different temperature were investigated. The dependence of the sensitivity of tungsten oxide nanowires to the methane as a function of the time was obtained. The sensitive properties of the tungsten oxide nanowires have almost linear relationship with the temperature.

1. INTRODUCTION

Over the last decade, nanostructured tungsten oxide materials have attracted much interest due to their potential for catalyst [1], gas sensors [2, 3], and electrochromic material applications [4]. Several studies have been conducted by using various techniques, including the oxygen plasma processing [5], plasma sputtering [6], chemical solution [7, 8], sol-gel techniques [9], electron beam evaporation deposition [10], electrochemical etching [11], and the chemical vapor deposition techniques [12]. Most work concerned the synthesis of nanoparticles for catalytic applications based on chemical solution methods [4, 7–9].

Using a simple hot filament CVD technique, we previously synthesized various nanostructured tungsten oxide (WO_3) films [13, 14]. The advantage of this technique was that both a.c. and d.c. electrical power supply could be used for heating the substrates. Low electrical power was used, less than 80 W. The temperature of the substrate was easily controlled by adjusting the distance between the substrate and the hot filament, and no extra heater was needed.

In the present work, we address ambient pressure syntheses of tungsten oxide nanoparticles and nanowires, and then the demonstration of their sensing applications. The main advantages of the ambient pressure deposition technique are that the temperature and density of plasma can be independently controlled during deposition. Furthermore, the experimental set-up is easy and effective, and the size of the sample is virtually unlimited. The effect of substrate temperature on the nanostructures of tungsten oxidefilms has also been investigated. Preliminary results of sensing material applications have been obtained.

2. EXPERIMENTAL SETUP

The nanostructured tungsten oxide materials were synthesized using a simple hot filament CVD technique. The details of the process were described elsewhere in our previous publications [13, 14]. The tungsten filament acted as a precursor for tungsten oxide, and no catalyst or other tungsten-containing compound precursor was used. Both AlN and Al_2O_3 ceramic substrates were used. Prior to the

experiments, the substrates were ultrasonically washed in the methanol solution for 5 minutes, and dried with helium. After placing the substrate, the chamber was pumped down to 2.0×10^{-5} Torr and then fed with the Ar gas (purity: 75%) to ambient pressure. During deposition, the gas inside the chamber was in a static state. The distance between the hot filament and substrate remained unchanged. The substrate temperature was controlled by adjusting electrical current on the hot filament, which was different from our previous experiments where the substrate temperature was controlled by simply changing the distance between the substrate and the hot filament.

3. RESULTS AND DISCUSSIONS

3.1. Grows and characterizations

Figure 1 shows typical SEM images of the nanostructured tungsten oxide films deposited on the AlN substrates at the substrate temperature of (a) 400°C and (b) 1000°C, respectively. The experiments were conducted at ambient pressure and the duration for each sample was 30 minutes. Different morphologies were observed for different substrate temperatures, but otherwise identical growth conditions.

At 400°C, nanowires with an average diameter of about 200 nm and length of about 1 μm are uniformly distributed on the surface of sample (Figure 1(a)). Raising the substrate temperature to 1000°C, the submicrometer size, well-shaped particles appear (Figure 1(b)).

From the naked eyes, the color of sample at 400°C appears green and dull. In contrast, following growth of substrate temperature to 1000°C, slightly shiny surface was obtained. It should be mentioned that with further increase of substrate temperature, the color of obtained film would become white, and the particles on the surface of the substrate look like diamond particles, very shiny.

In general, the growth of thin film may follow three types of models: layer by layer growth of Franck and Van der Merwe (FM), initial layer growth followed by island growth of Stranski and Krastanov (SK), and the island growth of Volmer and Weber (VW). A determinant factor is the competition among the surface free energies of the overlayer E_o, the substrate E_s, and the overlayer/substrate interface free energy E_i. The common model is the case that the substrate free energies is low and $E_s < E_o + E_i$, where three dimensional island growth (VW) occurs [14]. The epitaxial growth of tungsten oxide was conducted, where the lattice constants differ from the AlN substrates, strains were introduced into the layer, which prevents epitaxial growth of thicker layers without defects [14]. Since we have large misfit between the film and the substrate, our case can possibly be considered as a VW model. Furthermore, the misfit in lattices between films and substrates can be enhanced with the increase of substrate temperature. Basically, the overlayer will grow with a stacking fault after a first coherent layer.When the film was much thicker than critical thickness, the initial smooth surface of the film will become the fractal-like structure, and eventually the thin film was transformed to nanoparticles shown in Figure 1.

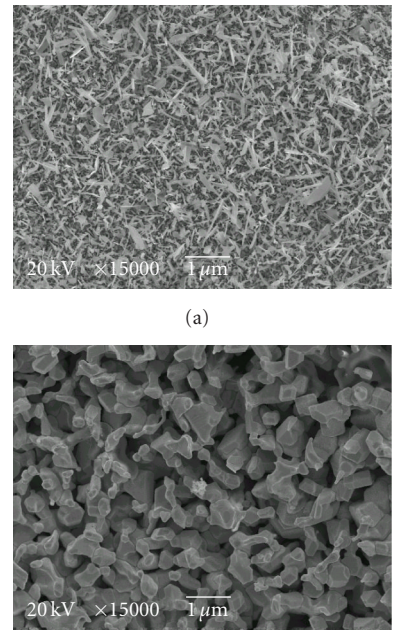

Figure 1: SEM images of the films prepared at substrate temperature of (a) 400°C and (b) 1000°C.

Energy dispersive X-ray spectroscopy (EDX) measurements were also conducted to quantitatively analyze the chemical composition of the tungsten oxide samples (shown in Figures 1(a) and 1(b)). The oxygen and tungsten atom concentrations are approximately 62.47 at% and 30.21 at%, respectively, for the first sample (Figure 1(a)). For the second one (Figure 1(b)), the oxygen concentration drops down to 55.78 at%, whereas the relative tungsten content increases up to 41.62 at%. The oxygen and tungsten concentration decreases from 2.07 to 1.34 from 400°C to 1000°C.

Clearly, the concentration ratio O/W is high at low temperature of deposition. With the increase of the substrate temperature, the concentration ratio O/W decreases, probably resulting in a significant effect on the crystalline structures and the phase of the present two samples. In fact, the following XRD data have also shown distinct properties related to relative oxygen content inside the films.

Figure 2 shows XRD patterns of the two tungsten oxide samples in Figures 1(a) and 1(b). WO_2, WO_3, and W peaks in XRD spectra of the films have been identified based on the literatures [15, 16]. The present two samples exhibit mixed states including WO_2, WO_3, and W. The polycrystalline WO_3 dominates the composition of the sample prepared at 400°C. Evidence is that XRD peaks of WO_3 with (002) and (200) orientations are much stronger than those of WO_2 and W peaks. At 1000°C, WO_2 signals remain nearly unchanged but the W components become dominant with the vanishing of WO_3 components. The XRD profiles of the films provide the direct evidence that the states of tungsten oxide films transfer from polycrystalline WO_3 domination to polycrystalline W domination.

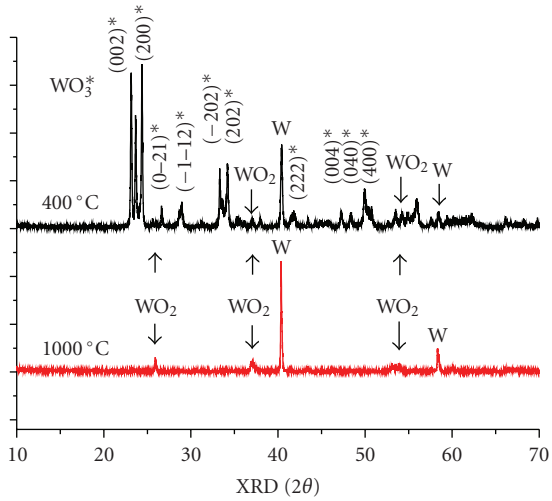

FIGURE 2: XRD of the tungsten oxide films corresponding to the samples shown in Figure 1.

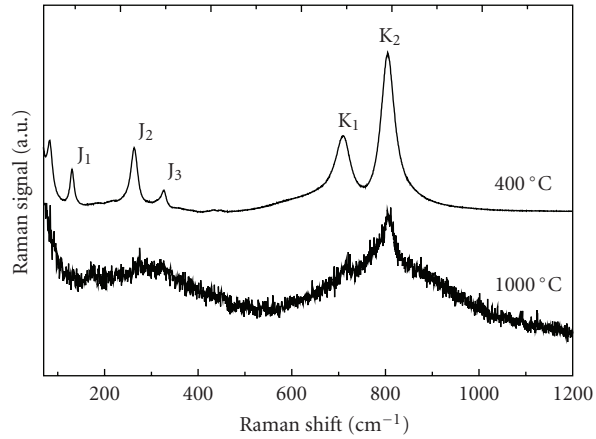

FIGURE 3: Raman spectra of the films at 400°C and 1000°C.

Raman scattering spectra of the tungsten oxide films were also obtained at room temperature by using a triple monochromator (ISA J-Y Model T64000) with an excitation wavelength of 514 nm (Ar^+ ion laser). The samples were scanned from 50 cm^{-1} to 1200 cm^{-1}. Several peaks marked with J and k in the Raman spectra were identified, respectively. In general, the bands situated at around 700 and 800 cm^{-1} can be assigned to W-O stretching models, whereas the bands situated at around 130 and 270 cm^{-1} are associated to W-O bending modes of monoclinic WO_3 [16, 17]. It was also reported that J bands at 270 and 330 cm^{-1} can also be assigned to W-O bending modes of monoclinic WO_3 [18]. According to our case, J_1, J_2, and J_3 bands in Raman spectra of all our tungsten oxide samples always coexist. Therefore, the present three bands have been assigned to J-bands associated to W-O bending modes of monoclinic WO_3.

Setting substrate temperature up to 1000°C, both K bands and J bands were obviously broadened, and their signal-to-noise ratios greatly reduced, suggesting changes of states of the samples. This is in agreement with the data obtained from XRD above. A shoulder close to higher wave number of WO_3K bands is also clearly visible. According to literature, this shoulder (Raman band) should be related to the contribution from W component [16].

Slightly blue shifts of k bands from 711 to 719 cm^{-1} for k_1 and from 806 to 808 cm^{-1} for k_2 following an increase of the substrate temperature from 400 to 1000°C have been observed from Figure 3. Generally, the blue shifts of the Raman peaks probably result from the change in crystal symmetry or the high stress of the particles. The variations of content of WO_2 and W inside unavoidably change crystal symmetry of WO_3. However, referring to the previous work [19], the stress due to mismatch and the different thermal expansion between the substrate and overlayer is qualitatively associated with increasing the shift and width of the band. The blue shifts of the samples are also due to the high stress of particles caused by the high temperature's deposition process.

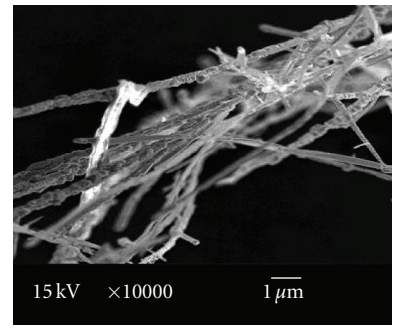

(a)

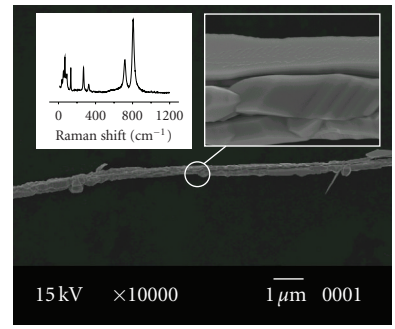

(b)

FIGURE 4: SEM images and Raman spectrum of the super long tungsten oxide wire-type nanostructures deposited on Al_2O_3 substrates at ambient pressure at 1000°C.

Besides, it was found that different substrate materials also affected the tungsten oxide structures. Figure 4 shows the super long tungsten oxide nanowires deposited on Al_2O_3 substrates at ambient pressure with the substrate temperature 1000°C. Bundles of wire-type tungsten oxide nanostructures with a length of up to 5 mm are distributed on the surface of Al_2O_3 substrate (Figure 4(a)). The average diameter of the nanowires is around 850 nm.

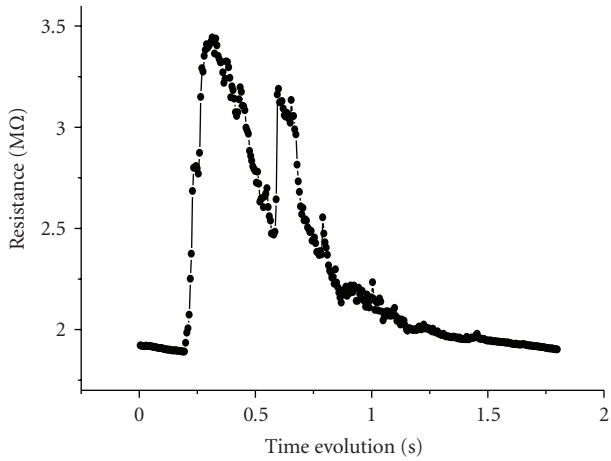

Figure 5: Evolution of sensitivity of nanowires after spraying methane gas.

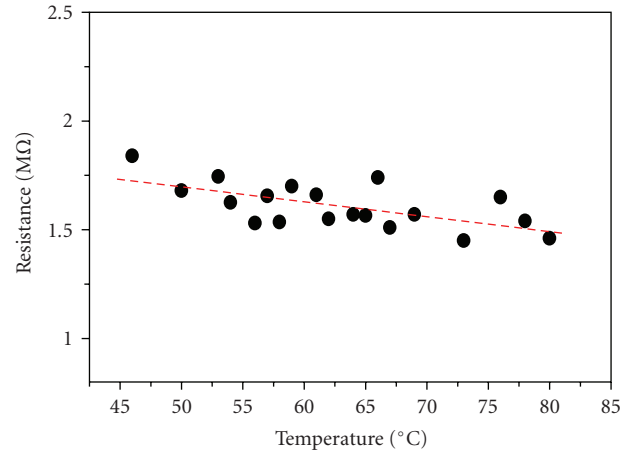

Figure 6: Variation of resistance of nanowires following the increase of temperature.

From SEM images in Figure 4, it can be observed that each wire consists of good-shaped segments. Typical WO_3 Raman spectrum has been obtained. The bands situated at 717.8 and 806.5 cm^{-1} are assigned to W-O stretching models, whereas the bands situated at 133.9, 272.1, and 327.3 cm^{-1} are associated to W-O bending modes of monoclinic WO_3. The synthesis of super long tungsten oxide nanowires are probably related to the chemical reactions between the Al_2O_3 substrates and the tungsten oxide materials.

3.2. The sensitive properties

Furthermore, the sensitive properties of the super long nanowires were also investigated as an example. A prototypic sensor was constructed, which consisted of a voltage-current-resistor (V-I-R) electrical circuit. The tungsten oxide nanowires were serially connected to a precise resistor and a power supply. The variations of the voltage across the precise resistor were detected by using WaveSurfer 452 oscilloscope LeCroy Inc. (NY, USA), from which the variations of resistances or conductivities of tungsten oxide nanowires could be estimated. The measurements of the electrical conductivity were conducted in order to understand the variations of the sensitive properties of the sensor at different conditions.

For traditional sensors, a disadvantage is that the sensitivity of the sensor mainly relies on the operating temperature. The extra heater installed inevitably leads to the complicated geometry of the prototypic sensor [20, 21]. The following measurements were conducted at room temperature, and the sensitivity of the prototypic sensor to the gas was obtained.

A spraying nozzle was used to eject liquid methane as fine particles or gas to the surface of the nanowires. Flow distribution was determined by gas (air) and liquid superficial velocities. The electrical conductivities of the sensor during the whole process were recorded by National Instruments LabVIEW software.

The dependence of the sensitivity of tungsten oxide nanowires as a function of the time is shown in Figure 5. The response time (rise time) is about 90 ± 0.5 milliseconds, and recovery time of the sensor is around 550 ± 0.5 milliseconds, which depends on the solvent, gas, liquid superficial velocities from spraying nozzle, and spraying duration.

After heavily spray of liquid methane, an obvious multipeak type of sensitive variation would be observed, which was possibly caused by piston vibration inside the valve. Similar phenomenon was observed in our previous supersonic atomic beam experiments [22]. In general, the width and density of the second peak in the pulsed atomic beam profile are much smaller than the first one. Meanwhile, a weak spray would yield a single peak of molecular pulse, which consequently led to the weak response signal of the prototypical sensor.

Figure 6 shows the dependence of the resistance of tungsten oxide nanowires as a function of temperature. Clearly, the resistance of nanowires reduces from 1.75 MΩ to 1.49 MΩ with an increase of the temperature from 45°C to 80°C under atmosphere condition. Signal output of the prototypical sensor has almost linear relationship with the temperature.

4. CONCLUSIONS

Tungsten oxide nanoparticles and nanowires were synthesized at ambient pressure on AlN substratesusing the hot filament CVD techniques. The amount of 400°C of deposition yields WO_3 film consisting of nanowires with an average diameter and length of about 200 nm and 1 μm, respectively. Increasing substrate temperature results in submicrometer size particles. The profiles of XRD of the films provide evidence of the mixture state changes from polycrystalline WO_3 domination to polycrystalline W domination. Typical EDX measurements of the films indicated that the concentration ratio O/W decreases from 2.07 to 1.34 from 400°C to 1000°C. Up to 5 mm super long tungsten oxide nanowires with diameter of about 850 nm

were obtained on Al_2O_3 substrate at 1000°C, but otherwise identical growth condition.

Experiments have proved that tungsten oxide nanowires can be used for sensing applications. The resistance of nanowires reduces from 1.75 MΩ to 1.49 MΩ with an increase of the temperature from 45°C to 80°C under atmosphere condition. After spray of liquid methane, the rise time of the signal is about 90 milliseconds, and the recovery time for the sensor is around 550 milliseconds.

ACKNOWLEDGMENTS

This work was partially supported by NSF (DMR-0706147) and DoD (W911NF-07-1-0014). The authors would like to thank Mr. William for assistance of Raman measurements, and Mr. Josuel for SEM and EDX measurements.

REFERENCES

[1] I. E. Wachs, T. Kim, and E. I. Ross, "Catalysis science of the solid acidity of model supported tungsten oxide catalysts," *Catalysis Today*, vol. 116, no. 2, pp. 162–168, 2006.

[2] V. Khatko, G. Gorokh, A. Mozalev, et al., "Tungsten trioxide sensing layers on highly ordered nanoporous alumina template," *Sensors and Actuators B*, vol. 118, no. 1-2, pp. 255–262, 2006.

[3] F. Galléa, Z. Li, and Z. Zhang, "Growth control of tungsten oxide nanostructures on planar silicon substrates," *Applied Physics Letters*, vol. 89, no. 19, Article ID 193111, 3 pages, 2006.

[4] C.-Y. Kim, J.-W. Choi, T.-Y. Lim, and D.-K. Choi, "Synthesis of WO_3 electrochromic sensor by sol-gel method and characterization of its electrochemical and optical properties," *Key Engineering Materials*, vol. 317-318, pp. 807–810, 2006.

[5] A. Romanyuk, R. Steiner, V. Melnik, and V. Thommen, "Ultrasound-assisted oxidation of tungsten in oxygen plasma: the early stages of the oxide film growth," *Surface and Interface Analysis*, vol. 38, no. 8, pp. 1242–1246, 2006.

[6] X. G. Wang, Y. S. Jang, N. H. Yang, L. Yuan, and S. J. Pang, "XPS and XRD study of the electrochromic mechanism of WO_x films," *Surface and Coatings Technology*, vol. 99, no. 1-2, pp. 82–86, 1998.

[7] F. Di Fonzo, A. Bailini, V. Russo, et al., "Synthesis and characterization of tungsten and tungsten oxide nanostructured films," *Catalysis Today*, vol. 116, no. 1, pp. 69–73, 2006.

[8] M. Deepa, A. K. Srivastava, and S. A. Agnihotry, "Influence of annealing on electrochromic performance of template assisted, electrochemically grown, nanostructured assembly of tungsten oxide," *Acta Materialia*, vol. 54, no. 17, pp. 4583–4595, 2006.

[9] M. Deepa, P. Singh, S. N. Sharma, and S. A. Agnihotry, "Effect of humidity on structure and electrochromic properties of sol-gel-derived tungsten oxide films," *Solar Energy Materials and Solar Cells*, vol. 90, no. 16, pp. 2665–2682, 2006.

[10] T. Nanba and I. Yasui, "X-ray diffraction study of microstructure of amorphous tungsten trioxide films prepared by electron beam vacuum evaporation," *Journal of Solid State Chemistry*, vol. 83, no. 2, pp. 304–315, 1989.

[11] G. Gu, B. Zheng, W. Q. Han, S. Roth, and J. Liu, "Tungsten oxide nanowires on tungsten substrates," *Nano Letters*, vol. 2, no. 8, pp. 849–851, 2002.

[12] R. G. Palgrave and I. P. Parkin, "Chemical vapor deposition of titanium chalcogenides and pnictides and tungsten oxide thin films," *New Journal of Chemistry*, vol. 30, pp. 505–514, 2006.

[13] X. P. Wang, B. Q. Yang, H. X. Zhang, and P. X. Feng, "Tungsten oxide nanorods array and nanobundle prepared by using chemical vapor deposition technique," *Nanoscale Research Letters*, vol. 2, no. 8, pp. 405–409, 2007.

[14] P. X. Feng, X. P. Wang, H. X. Zhang, et al., "Study of the structural evolutions of crystalline tungsten oxide films prepared using hot-filament CVD," *Journal of Physics D*, vol. 40, no. 17, pp. 5239–5245, 2007.

[15] Yu. S. Krasnov, S. V. Volkov, and G. Ya. Kolbasov, "Optical and kinetic properties of cathodically deposited amorphous tungsten oxide films," *Journal of Non-Crystalline Solids*, vol. 352, no. 38-39, pp. 3995–4002, 2006.

[16] Z. Lu, S. M. Kanan, and C. P. Tripp, "Synthesis of high surface area monoclinic WO_3 particles using organic ligands and emulsion based methods," *Journal of Materials Chemistry*, vol. 12, no. 4, pp. 983–989, 2002.

[17] K. Nonaka, A. Takase, and K. Miyakawa, "Raman spectra of sol-gel-derived tungsten oxides," *Journal of Materials Science Letters*, vol. 12, no. 5, pp. 274–277, 1993.

[18] Z. Xiao, L. Zhang, X. Tian, and X. Fang, "Fabrication and structural characterization of porous tungsten oxide nanowires," *Nanotechnology*, vol. 16, no. 11, pp. 2647–2650, 2005.

[19] Y. Shigesato, A. Murayama, T. Kamimori, and K. Matsuhiro, "Characterization of evaporated amorphous WO_3 films by Raman and FTIR spectroscopies," *Applied Surface Science*, vol. 33-34, pp. 804–811, 1988.

[20] Y. S. Kim, S.-C. Ha, K. Kim, et al., "Room-temperature semiconductor gas sensor based on nonstoichiometric tungsten oxide nanorod film," *Applied Physics Letters*, vol. 86, no. 21, Article ID 213105, 3 pages, 2005.

[21] V. Khatko, E. Llobet, X. Vilanova, et al., "Gas sensing properties of nanoparticle indium-doped WO_3 thick films," *Sensors and Actuators B*, vol. 111-112, pp. 45–51, 2005.

[22] P. X. Feng and B. Weiner, "A collimated pulsed supersonic metastable helium atomic beam," *Physica Scripta*, vol. 75, no. 4, pp. 565–571, 2007.

Hindawi Publishing Corporation
Journal of Nanomaterials
Volume 2008, Article ID 429168, 9 pages
doi:10.1155/2008/429168

Research Article

Modeling and Formulation of a Novel Microoptoelectromechanical Gyroscope

Bohua Sun, Bo Zhang, and Mohamed Toriq Khan

Centre for Mechanics, Smart Structure and Micro-Systems, Cape Peninsula University of Technology, Cape Town 7535, South Africa

Correspondence should be addressed to Bohua Sun, sunb@cput.ac.za

Received 20 February 2008; Accepted 12 May 2008

Recommended by Rakesh Joshi

This paper proposed a novel design of microgyroscope based on MEMS structures and optic interferometric microdisplacement measurement technique. The gyroscope consists of microvibrator and interferometric readout. Using Coriolis force, the vibrator transfers the system rotation into a forced vibration; the induced vibration can be sensed by the interferometric microdisplacement measurement system. The optic measurement system has two mirrors which will reflect two rays into a detector. The comprehensive studies on the formulation and analysis of the proposed gyroscope have been undertaken; two key sensor equations have been derived in the first time in the world: (1) relation between rotation and phase shift of light $\Delta\varphi = (4\pi l_0/\lambda) + (8\pi/\lambda)(x_{\max}Q_y/\omega_y)\Omega(t)\sin(\omega_d t)$, (2) relation between rotation and interferometric intensity of light $I(t) \approx (8\pi/\lambda)(x_{\max}Q_y/\omega_y)\Omega(t)\sin(\omega_d t)\sin(4\pi l_0/\lambda)$. The comparison of the proposed gyroscope and well-know Sagnac formulation has been investigated; it shown that the proposed model is much better than Sagnac ones. The new model has finally get rid of needing very long fiber in the case of Sagnac gyroscope. The innovative model gives a new hope to fabricate high accurate and cheaper gyroscope. To date, the proposed gyroscope is the most accurate gyroscope.

1. INTRODUCTION

Gyroscopes are the inertial measurement devices, which are used to detect angular rotation rate of the objects. which are widely used for guidance, navigation, airplanes, spacecrafts, missiles, automobiles, and even consumer electronics to maintain orientation, measure the angular motion of essential objects for the control and stabilization of its attitude.

The gyroscope development is going through the processes from the macrosize to the microsize. Traditional gyroscopes with spinning wheels employed in the present aerospace and military industries are bulky, which need lubricant and wear out, as stability control system, navigation system, and so forth. Ring laser gyroscopes (RLGs) and fiber optical gyroscopes (FOGs) are high precision. But they are expensive and heavy. The micro applications require the host structures to be transformed from the huge spin wheel mass to the tiny light vibration mass or optical interferometer measurement system fabricated by microelectromechanical system (MEMS) technology like MEMS vibratory gyroscopes and fiber optical gyroscopes [1].

In terms of small size critical, MEMS vibratory gyroscopes are the perfect substitution, especially for microsatellites, microunmanned vehicles, digital cameras, and notebook, PDA, due to their small size. MEMS gyroscopes are also suitable for longtime employ because of low power consumption, and the bulk fabrication processes can produce batch applications. Since the light weight and low power consumption, some small instruments like digital cameras can wear several MEMS gyroscopes and accelerometers for positioning or monitoring its activities either in vehicle or out of vehicle during travel [2]. In fact, some types of sell MEMS gyroscopes have started for dynamic control of automobiles a few years ago. Silicon basement sensing system is providing MEMS gyroscopes by Analog Devices.

Silicon-based MEMS gyroscopes processes may be categorized into bulk micromachining and surface micromachining. A large mass is desired for a gyroscope because thermomechanical noise is inversely proportional to mass weight. Generally, MEMS gyroscopes and bulk micromachined gyroscopes have large mass and relatively large

readout capacitance or piezoresistive readout. Therefore, most bulk bonding to a separate electronic readout chips (two chips). Two chips gyroscopes are expensive and have a relatively large package size that restricts their applications in consumer electronics regardless of price. In contrast, surface micromachining gyroscopes have small mass and relatively small readout capacitance. The sensors and readout electronics are usually integrated on a single chip to reduce parasitic capacitance and size.

MEMS gyroscopes system can only sense in one axis, but angular rate is requiring a vector, measuring all three-axis rotations. Assembling three gyroscopes together is needed, which will increase the package size, and the complexity of packaging cost. The capacitance readout electronic circuits have the essential shortcoming at the sensitivity, responding time, bandwidth, and so forth. Therefore, the current MEMS gyroscopes only occupy the low and middle sensitivity scales markets.

On the other hand, many intrinsic optical theories are used in the new field for pressure, temperature, acceleration, skin friction sensors, and so forth, and the performances of optical sensors and measurements scale are better than mechanical sensors or others at sensitivity, volumes, cost, stability, and so forth. Optical type gyroscopes have advantages at the sensitivity, performance, responding time, lifetime, and bandwidth. They occupy the high sensitivity and performance markets. Ring laser gyroscopes, fiber optical gyroscopes, and other optical gyroscopes are too large and heavy for many applications due to the Sagnac effect principle, which is the basic theory for all kinds of optical gyroscopes. The large size comes from the long distance light path to create the enough interference and the lack of MEMS fabrication technology for the micro-optical devices.

However, the MEMS inertial sensors have the following advantages compared with the conventional inertial instruments [3].

(1) Smaller volume and lighter weight

The advanced semiconductor manufacturing processes make the volume smaller and the weight of the microinertial mechanical sensors lighter.

(2) Mass production and lower production cost

Thousands of microinertial devices in a 3 inch or 4 inch silicon chip could be yielded with the mature technique and batch production, which will improve the rate of finished products and reducing the cost. The cost of microinertial devices, then, will depend on the packaging, testing, and accessory circuits. It is undoubted that the cost would drop greatly when the true integration of electromechanical is accomplished.

(3) Antiharsh environments and wider applications

With the small testing proof mass, a micromechanical accelerometer is adapted to measure the high acceleration.

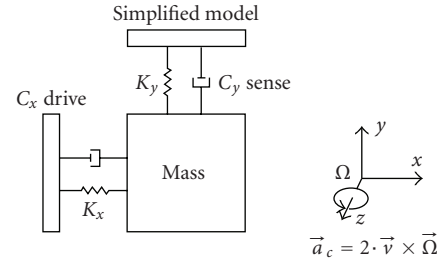

Figure 1: Model of coriolis force.

The measurement range could be extended widely by the micromechanical gyroscopes without rotating parts.

(4) Lower consumption, higher sensitivity and efficiency

When performing the same task, the consumption of micromechanical devices is only one tenth of the traditional ones or even less, while the operation speed could be improved ten times. Certain reasons, for example, the no delay performance of integrated micromechanical devices results in their wide use in high-speed application.

(5) Multifunction and intelligence

Most micromechanical devices integrated the transducer, actuator, and electronic circuits. It is easier to realize the multifunction and intelligence of micromechanical devices after using the intelligent materials and structures.

The novel combination of the microvibratory gyroscope and optical interferometer readout system is proposed in this paper. The merged system has the small size and high performance and is suitable for MEMS fabrication technology. In this paper, the system design, mathematical model, and performance analysis are presented.

2. MICROMECHANICAL DESIGN OF THE MOEMS GYROSCOPE

Based on the comprehensive review of the optical gyroscopes and MEMS silicon-based gyroscopes, we propose a hybrid model which combine MEMS silicon-based oscillation gyroscopes and micro-optical interferometer readout system. It will take both advantages of MEMS vibratory gyros and optical sensing technique. It is believed that the proposed gyroscope can be massively fabricated with high performance at low cost.

The operation of the z-axis vibratory rate gyroscope is best illustrated by the spring-mass system shown in Figure 1. As in all vibratory rate gyroscopes, Coriolis acceleration is generated by an oscillating proof mass in a rotating reference frame. The proof mass is oscillated along the x-axis (the driven mode), the reference frame rotates around the z-axis, and the Coriolis acceleration is detected as deflections along the y-axis (the sense mode) [4].

The microelectromechanical sense element of the surface micromachined z-axis vibratory rate gyro is also shown in Figure 2. The structure comprises three major elements:

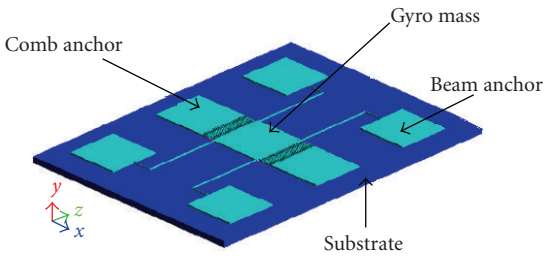

Figure 2: Solid model of MEMS vibratory structure.

the suspension system, the comb drive used to sustain oscillation, and the proof mass forced by the Coriolis force in y-axis.

Coriolis acceleration is

$$\vec{a_c} = 2 \cdot \vec{v} \times \vec{\Omega} \tag{1}$$

which shows that orthogonal lateral-axis vibration and acceleration sensing are required to detect the z-axis rotation. The mathematics principle model is shown in Figure 1.

One vibration mode corresponds to the vibration of mass in the x-direction with a vibration frequency of ω_x. The other vibration corresponds to the vibration of mass in the y-direction with a vibration frequency of ω_y [5, 6].

For operation, the mass is driven into vibration in the x-direction with a driving frequency ω_d.

Given driven signal,

$$x = A_d \sin \omega_d t. \tag{2}$$

Then, if the system rotates around the z-axis with a constant angular rate of Ω, the Coriolis force appears in the y-axis and impelling the mass vibrating in y-axis:

$$\begin{aligned} \dot{x} &= A_d \omega_d \cos \omega_d t, \\ F_c &= 2m\dot{x}\Omega. \end{aligned} \tag{3}$$

Differential equation for the mass movement in the y-direction is given by

$$m\ddot{y} + c_y \dot{y} + k_y y = 2mA_d \omega_d \Omega \sin\left(\omega_d t + \frac{\pi}{2}\right). \tag{4}$$

The steady-state solution is given by

$$y = A_y \sin\left(\omega_d t + \frac{\pi}{2} - \varphi\right) = A_y \cos(\omega_d t - \varphi). \tag{5}$$

There, amplitude at y-direction is

$$A_y = \frac{2A_d \omega_d \Omega}{\omega_y^2 \sqrt{\left(1 - \omega_d^2/\omega_y^2\right)^2 + 4\zeta_y^2 \left(\omega_d^2/\omega_y^2\right)}}. \tag{6}$$

Phase is

$$\begin{aligned} \varphi &= \tan^{-1} \frac{2\zeta_y \omega_d \omega_y}{\omega_y^2 - \omega_d^2}, \\ \zeta_y &= \frac{c_y}{2m\omega_y}, \end{aligned} \tag{7}$$

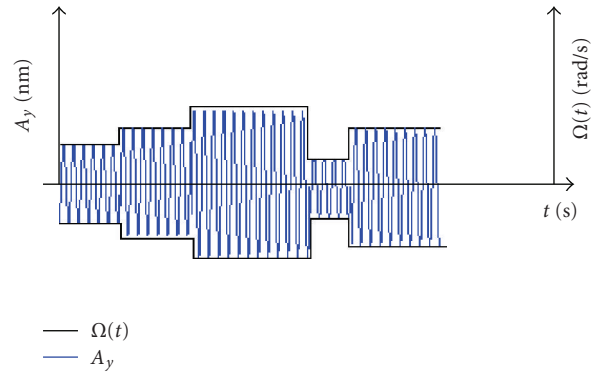

Figure 3: Oscillating coriolis displacements creating by variable rotation velocity.

where Q_y is the quality factor at the sensing mode given by

$$Q_y = \frac{1}{2\zeta_y}. \tag{8}$$

Let $\omega_d = \omega_y$, the mass amplitude becomes at resonance

$$A_y = \frac{2A_d \Omega Q_y}{\omega_y} = \frac{2A_d Q_y}{\omega_y} \Omega. \tag{9}$$

Equation (9) shows that the measurement of rotation Ω can be achieved by sensing the amplitude of vibration in y-direction, the problem of measurement of rotation becomes a problem of sensing a displacement. It is the foundation of vibratory gyroscope principle.

The system response froced Coriolis acceleration along y-axis is given by (9).

The vibration along y-axis is

$$\frac{y}{\Omega} = \frac{2A_d Q_y}{\omega_y} \sin\left(\omega_d t + \frac{\pi}{2} - \varphi\right). \tag{10}$$

The results of the relative between the angular rate and Coriolis acceleration are clear, which shows the y-axis amplitude proportion with the z-axis angular rate, and the x-axis driver oscillation redound to amplifier the amplitude of the y-axis [7]. In the microsize, the nature frequency of oscillation beams and proof mass is very high, and the weight is very light. It is of the advantage driving the mass at the x-axis under low power consumption, and achieves the high sensitivity.

Now, the angular rate measurements convert to measure the y-axis amplitude, shown in Figure 3. This changing gives the measurement idea, which is microdisplacement measurement. There are many methods to measure microdisplacements like bridge resistance, bridge capacitance, piezoelectricity, optical modulation methods, and so forth. Currently, the optical interferometer is the most precise method, which is the method proposed in this paper.

3. MICRO-OPTICAL INTERFEROMETRIC DESIGN OF THE MOEMS GYROSCOPE

From (9), we know that the problem of measurement of rotation becomes a problem of sensing a displacement. There

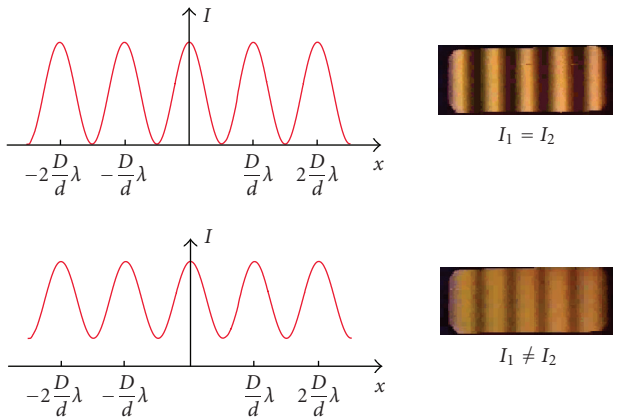

Figure 4: Interferometer output intensity and patterns.

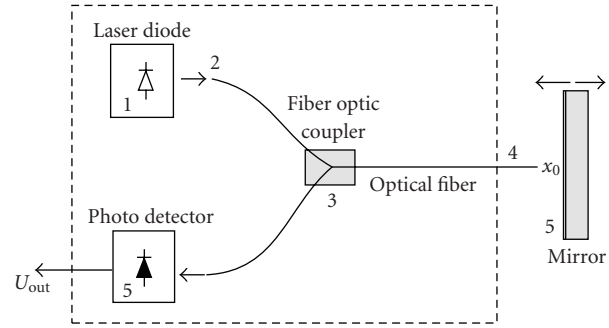

Figure 5: Diagram of micro fiber optical interferometer.

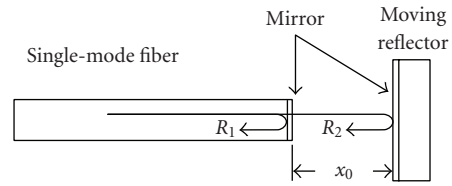

Figure 6: Magnify fiber optic interferometer head.

are several ways to sense the displacement, but up to now the optic sensing is the most accurate one.

The optical interferometric readout system has the high sensitivity, high precision, high integration, low cost characteristics. Interference, which is a complex wave phenomenon, is one of the useful readout, which can be happened and observed in frequency wave areas, like the mechanical wave, sound wave, light wave, electric wave, and so forth [8]. In the optical technology, the interference will be happened under those situations, no matter the sensor is a Michelson, a Mach-Zehnder, a Sagnac, or a Fabry-Perot interferometer, (1) frequency of two beams must be same; (2) the vibration of two beams must be same direction; (3) phase shift of two beams must be holed constant.

The intensity of general interferometer output is composition of two light beams I_1 and I_2:

$$I = I_1 + I_2 + 2\sqrt{I_1 I_2}\cos\varphi_{12}. \tag{11}$$

Here, φ_{12} is the phase shift different of two beams at interaction point:

$$\varphi_{12} = \varphi_1 - \varphi_2 - 2\pi\frac{\Delta L}{\lambda}. \tag{12}$$

Here φ_1 and φ_2 are initialization phase of two beams. ΔL is the path-length different of two beams.

The periodic intensity patterns are shown in Figure 4.

The phenomenon of the interference of light underlies many high-precision measuring systems and displacement sensors. The use of optical fibers allows making such devices extremely compact and economic. In fiber optic interferometer, the interference occurs at the partially reflecting end face surface of the fiber and an external mirror. The size of the sensitive element based on this principle can be as small as diameter of the fiber, and the sensitivity can achieve subangstrom level. Additionally, such sensor is not sensitive to electromagnetic interference and can be used in hostile environment.

Consider the principle of operation of the fiber optic interferometer, the system view shown in Figure 5, and the magnifying sensor head configurations shown in Figure 6.

The radiation of the laser diode 1 is coupled into fiber 2 and propagates through coupler 3 to fiber 4. Then, one part of radiation is reflected from the end face of fiber 4, and other part of radiation is flashed into the air, reflected from the mirror 5 and returned back into fiber 4. The optical beam reflected from the end face of fiber 4 interferes with the beam reflected from the mirror. As a result, the intensity of the optical radiation at photodetector 5 is periodically changed depending on the distance x_0 between the fibers and mirrors as follows. The path-length difference is $\Delta L = 2x_0$.

The out intensity is

$$I = I_1 + I_2 + 2\sqrt{I_1 I_2}\cos\left(\frac{4\pi}{\lambda}x_0 + \varphi_0\right). \tag{13}$$

Here, φ_0 is initialization phase shift. λ is the wavelength of the light source used; phase shift is $\Delta\varphi = (2\pi/\lambda)\Delta L = (4\pi/\lambda)x_0$; I_1 and I_2 are intensities of these two reflected rays.

In fiber optic interferometer, $I_1 = I_0 R_1$ is the intensity of the light reflected from the end face surface of the fiber, and $I_2 = (1 - R_1)^2 R_2 I_0$ is the intensity of the light reflected from an external mirror and returned back into the fiber, where I_0 is the intensity of the laser diode radiation coupled into the fiber, R_1 is the reflectivity of the end face of the fiber, and R_2 is the reflectivity of an external mirror. Figure 7 shows the simulation result of the relationship between sensor output I_0/I and gap distance x_0. This gap distance x_0 is the position to setup the movement reflected surface, which is also the definition of the interferometer cavity length [9, 10]:

$$I = I_0\left[R_1 + (1-R_1)^2 R_2 + 2(1-R_1)\sqrt{R_1 R_2}\cos\left(\frac{4\pi}{\lambda}x_0 + \varphi_0\right)\right], \tag{14}$$

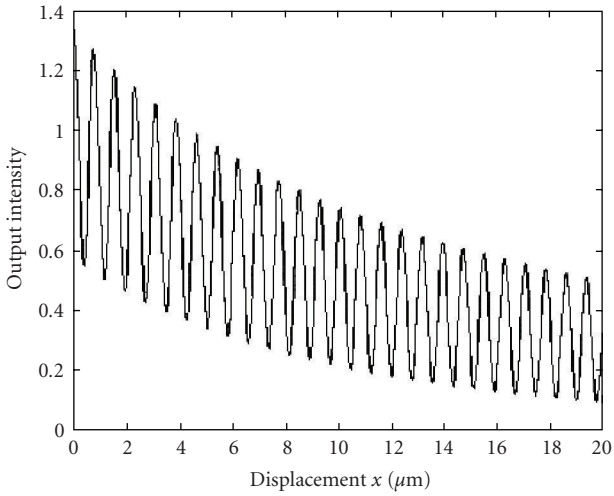

Figure 7: Simulation result of the relationship between sensor output I_0/I and gap distance x.

in which $I_1 = I_0R_1$ and $I_2 = (1 - R_1)^2R_2I_0$ are constant, by applying demodulation technique, the above equation (14) can be simplified as

$$I \approx \cos\left(\frac{4\pi}{\lambda}x_0 + \varphi_0\right). \tag{15}$$

For simplification and cavity design purpose, let $x_0 = k\lambda/2$, and $\varphi_0 = 0$, then we have

$$\begin{aligned} \Delta\varphi &= \frac{4\pi}{\lambda}x_0 = 2k\pi, \quad k = 0, \pm1, \pm2, \ldots, \\ I_{\max} &= \left(\sqrt{I_oR_1} + \sqrt{(1 - R_1)^2R_2I_o}\right)^2. \end{aligned} \tag{16}$$

Let $x_0 = (\lambda/4)(2k + 1)$,

$$\begin{aligned} \Delta\varphi &= \frac{4\pi}{\lambda}x_0 = (2k + 1)\pi, \quad k = 0, \pm1, \pm2, \ldots, \\ I_{\min} &= \left(\sqrt{I_oR_1} - \sqrt{(1 - R_1)^2R_2I_o}\right)^2. \end{aligned} \tag{17}$$

From the above intensity distributing analysis, as every time the cavity length x_0 is changing $\lambda/4$, the intensity would be varied from maxima to minima.

So the movement distance can be calculated by

$$\Delta S = \frac{\lambda}{4}N. \tag{18}$$

Here, ΔS is the distance moving from initialization position x_0. N is the times of the intensity changing.

Let $\varphi_0' = (4\pi/\lambda)x_0$ be presenting cavity x_0 equivalent initialization phase shift. The initialization phase φ_0' is located at the middle of $I_{\max}$ and $I_{\min}$, because here is maxima linear slope, shown in Figure 8. For microdisplacement, the accurate output result can be achieved in this linear region. The initialization position for movement reflected surface is

$$\begin{aligned} x_0 &= \frac{k\lambda}{8}, \\ I_{x_0} &= \frac{I_{\max} - I_{\min}}{2}. \end{aligned} \tag{19}$$

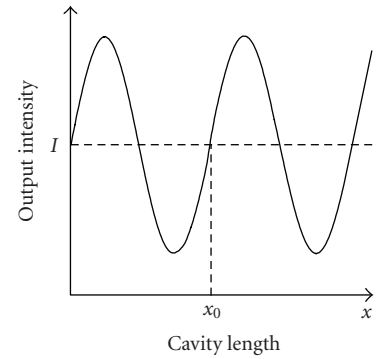

Figure 8: Initialization position of the vibratory reflected surface and linear region.

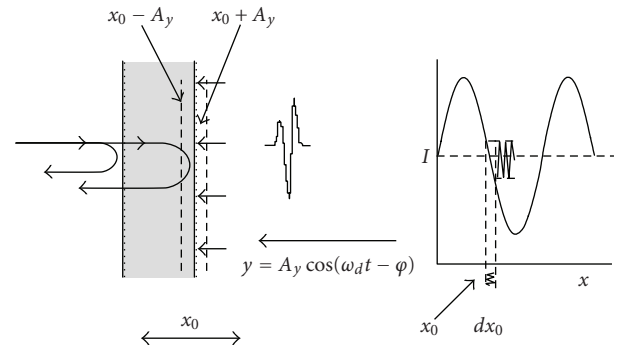

Figure 9: Effecting oscillation input to output intensity.

Now, we will consider the interferometric signal appearing as a result of the reflection of the light from the vibrating surface (resonator). When the resonator oscillates, the phase difference of interfering rays is varied as follows. The principle diagram shown in Figure 9 is describing the affection oscillation input to output intensity of the microfiber optical interferometer. The distance measurement performance of the micro-optical fiber interferometer is proved under 5 nm [11, 12].

According to the Coriolis acceleration theory, the y-axis vibration created by z-axis ration rate is

$$y = A_y \sin\left(\omega_d t + \frac{\pi}{2} - \varphi\right) = A_y \cos(\omega_d t - \varphi). \tag{20}$$

Path-length difference is

$$\begin{aligned} \Delta L &= 2[x_0 + A_y \cos(\omega_d t - \varphi)], \\ \Delta\varphi &= \frac{4\pi}{\lambda}[x_0 + A_y \cos(\omega_d t - \varphi)]. \end{aligned} \tag{21}$$

This $A_y\cos(\omega_d t - \varphi)$ vibration signal gives rise to the following modulation of the light intensity:

$$\begin{aligned} I(t) &\cong \cos\left\{\frac{4\pi}{\lambda}[x_0 + A_y \cos(\omega_d t - \varphi)]\right\} \\ &\cong \cos\left[\frac{4\pi}{\lambda}A_y\cos(\omega_d t - \varphi) + \frac{4\pi}{\lambda}x_0\right]. \end{aligned} \tag{22}$$

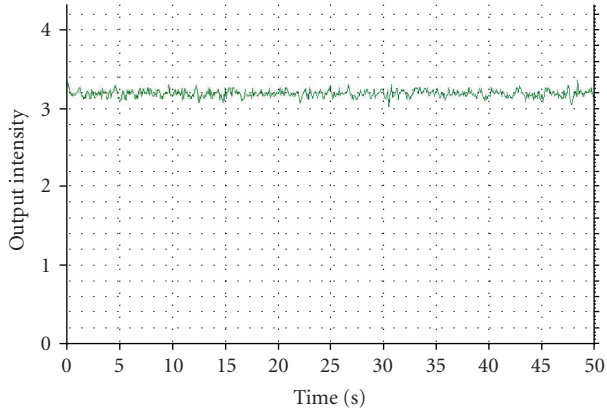

Figure 10: Output intensity at $\Omega = 0$.

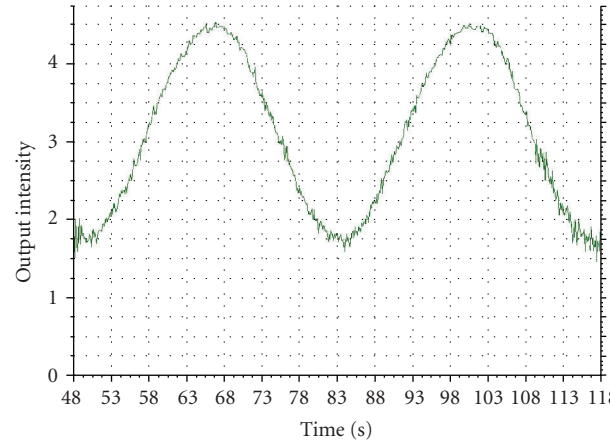

Figure 11: Output intensity at $\Omega \neq 0$ rad/s.

Expanding $I(t)$ in a Fourier series, and Bessel function $\cos(x \sin y) = J_0(x) + 2\sum_{n=1}^{\infty} J_{2n}(x) \cos 2ny$, the alternating components of the light modulation is:

$$I(t) \cong J_1(\varphi_\omega) \sin(\omega t - \eta) \sin \varphi_0' - J_2(\varphi_\omega) \cos(\omega t - \eta) \cos \varphi_0' + \cdots, \tag{23}$$

where $J_i(\varphi_\omega)$ is the Bessel functions, $\varphi_\omega = (4\pi/\lambda)A_y$. When $\varphi_\omega \ll 1$, then $J_i(\varphi_\omega)$ equals approximately $\varphi_\omega/2$ and, therefore, an alternating component of intensity $I(t)$ will be proportional to displacement of the resonator from the equilibrium: $I(t) \sim \sin(\omega t)$:

$$I(t) \cong \frac{1}{2}\varphi_\omega \sin(\omega t - \eta) \sin \varphi_0' \cong \frac{2\pi}{\lambda} A_y \sin \varphi_0' \cos(\omega_d t - \varphi). \tag{24}$$

Let $\omega_d = \omega_y$, the amplitude becomes

$$A_y = \frac{2A_d \Omega Q_y}{\omega_y} = \frac{2A_d Q_y}{\omega_y}\Omega, \tag{25}$$

$$I(t) \cong \frac{4\pi A_d Q_y}{\lambda \omega_y} \Omega \sin \varphi_0' \sin\left(\omega_d t + \frac{\pi}{2} - \varphi\right), \tag{26}$$

$$\Omega \cong \frac{I(t)\lambda\omega_y}{4\pi A_d Q_y \sin \varphi_0' \sin\left(\omega_d t + (\pi/2) - \varphi\right)}. \tag{27}$$

Let $\alpha = \lambda\omega_y / 4\pi A_d Q_y \sin \varphi_0'$,

$$\Omega \cong \alpha \frac{I(t)}{\cos(\omega_d t - \varphi)} = \alpha I(t) \cos^{-1}(\omega_d t - \varphi). \tag{28}$$

The linear displacement linked between the y-axis vibration in MEMS structure and the optical readout system is the key factor for the microopticelectromechanical gyroscope; the system model is in Figure 12. The vibration parameter is the requirement measurement, which is creating the intensity changing as well.

The relative parameters of the angular motion can be calculated by integrating (27). This results in the equation

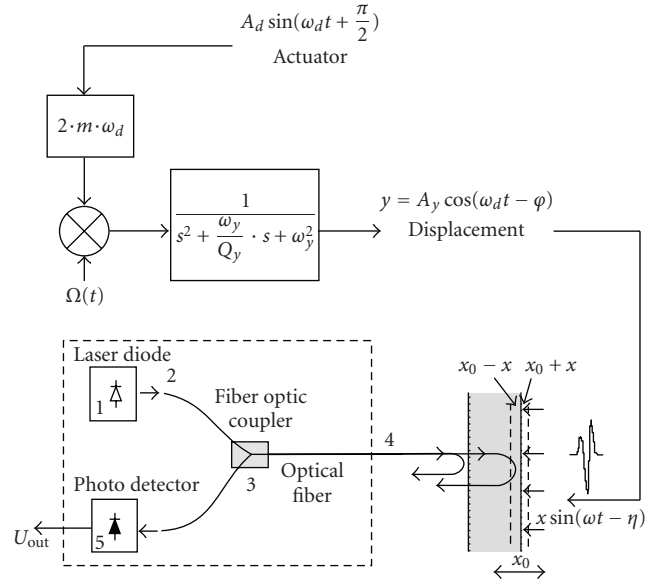

Figure 12: Model of micro vibratory optical readout gyroscope system.

below indicate angular displacement, θ, which is useful for navigation systems directly.

The angular movement is the integral of angular rate:

$$\Delta\theta = \int \Omega(t)dt = \alpha \int_{t1}^{t2} \frac{I(t)}{\cos(\omega_d - \varphi)} dt = \left[\alpha \frac{1}{\omega_d} \ln \left| \tan\left(\frac{\omega_d t}{2} + \frac{\pi}{4}\right)\right| + C\right] \int_{t1}^{t2} I(t)dt. \tag{29}$$

From (29), the operator of navigation would indicate the angular movement variation value $\Delta\theta = \theta_{t2} - \theta_{t1}$; feedback signal would emendate the application during the steering.

Therefore for any intensity readout, the angular movement value can be calculated as $\Delta\theta$ due to the reference frame, by means of a simple digital signal processor circuit attached to the optical readout of the MOEMS device.

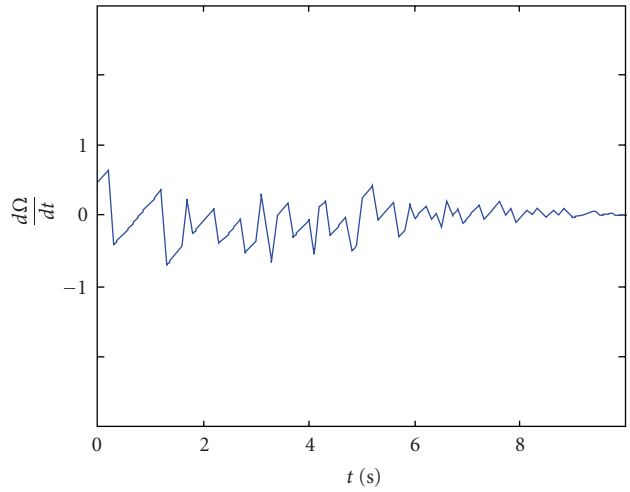

Figure 13: Angular acceleration attenuation diagram.

If (27) is differentiated, the rotation acceleration is obtained, shown in

$$\ddot{\theta} = \frac{d\Omega}{dt} = \alpha \frac{\dot{I}(t) + I(t)\omega_d \tan(\omega_d t - \varphi)}{\cos(\omega_d t - \varphi)}. \tag{30}$$

This is another useful output signal to control the system's stability. From (30), the signal is fast attenuation signal as the expectation. The application is illustrated in Figure 13.

4. MOEMS GYROSCOPE COMPARISON WITH OPTICAL GYROSCOPE BASED ON SAGNAC EFFECT

The Sagnac effect is the relative phase shift between two beams of light that have traveled an identical path in opposite direction in a rotating frame. The explanation of the Sagnac effect is simple for the inertial frame of reference. The motions of the mirrors, during the light transit time between mirrors, cause the clockwise and counterclockwise waves to be reflected at different points of space, which leads to an optical path difference. Modern fiber-optic gyroscopes (Sagnac interferometers) used for navigation are based on this effect. They allow highly accurate measurements of rotation rates down to about 0.1° per hour. The schematic setup of a Sagnac interferometer is shown in Figure 14. Light is decomposed into two beams by a 50:50 beam splitter, with one traveling clockwise (CW) and the other counterclockwise (CCW) around a polarization-maintaining single-mode glass-fiber loop. The two beams interfere after passage through the loop, and the interference signal is measured with a photodiode. If only reciprocal effects are involved in the experiment, then the two beams interfere constructively (relative phase shift $\Delta\phi = 0$). If $\Delta\phi \neq 0$, then nonreciprocal effects occur, one of them is the Sagnac effect that results from rotation of the fiber loop during the measurement.

The Sagnac effect is a relativistic effect but can be understood with a simple picture (see Figure 15). Let us assume that a fiber coil (N windings with radius R) is rotated

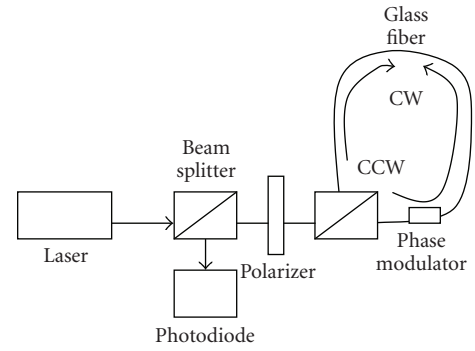

Figure 14: Schematic setup of a Sagnac interferometer.

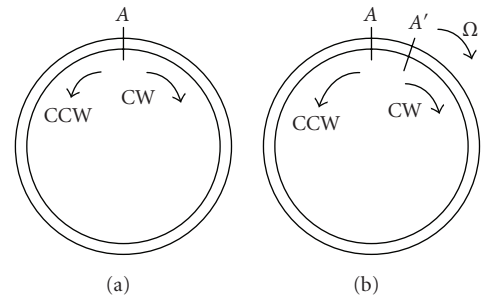

Figure 15: The Sagnac effect principle diagram.

clockwise with an angular velocity, and that light is injected into the loop at time $t = 0$. At $t_t \approx 2\pi RN/c$, the CW and CCW beams meet again at the starting point. However, due to the rotation of the loop, they have traveled in different path lengths. Figure 15 on the right indicates what happen if the loop itself is rotating during this procedure. Supposing that radius of fiber round is R, and light emitting and detector sensors are laid in "A" point. The system is rotating with Ω in the clockwise direction relatively inertia space. When clockwise direction light (CW) and the counter-clockwise direction light (CCW) are emitted in opposite direction around, the photo sensor also rotates from "A" to "A." So the two light paths have different length. The clockwise direction light pursues "A" after back, which crosses the distance more than $2\pi R$. While the counterclockwise direction light goes face to "A," which crosses the distance less than $2\pi R$. The difference between the travel times causes the difference light distance [13].

Assume light transmitting in vacuum, which velocity is $c = 3 \times 10^8$. The paths of clockwise and counterclockwise light are L_{CW}, L_{CCW}; spending time is t_{CW}, t_{CCW}, individually.

Let $C = C_{\mathrm{cw}} = C_{\mathrm{ccw}}$,

$$\begin{aligned} L_{\mathrm{cw}} &= 2\pi R + R\Omega t_{\mathrm{cw}} = C_{\mathrm{cw}} t_{\mathrm{cw}}, \\ L_{\mathrm{ccw}} &= 2\pi R - R\Omega t_{\mathrm{ccw}} = C_{\mathrm{ccw}} t_{\mathrm{ccw}}. \end{aligned} \tag{31}$$

From (1), Δt is

$$\Delta t = t_{cw} - t_{ccw} = 2\pi R \frac{2\pi\Omega - (C_{cw} - C_{ccw})}{C_{cw} \cdot C_{ccw}} = 2\pi R \frac{2\pi R\Omega}{C^2} = \frac{4A\Omega}{C^2}, \tag{32}$$

where A is area of ring fiber round.

Accounting, it is only approximate and simple evolvement above result in (32). The strict evolvement should be applied in broad theory of relativity. The speed of light transmitted in fiber optical depends on refractive index of medium.

So, clockwise and counterclockwise light is

$$C_{cw} = \frac{c/n + R\Omega}{1 + ((c/n)\cdot R\Omega)/c^2} = \frac{c/n + R\Omega}{1 + R\Omega/cn},$$
$$C_{ccw} = \frac{c/n - R\Omega}{1 - ((c/n)\cdot R\Omega)/c^2} = \frac{c/n - R\Omega}{1 - R\Omega/cn}, \tag{33}$$

where n is refractive index of medium. From (33), we have

$$\Delta t = t_{cw} - t_{ccw} = 2\pi R \frac{2\pi\Omega - (C_{cw} - C_{ccw})}{C_{cw} \cdot C_{ccw}} \approx 2\pi R \frac{2R\Omega - 2R\Omega(1 - (1/n^2))}{c^2/n^2} = 2\pi R \frac{2\pi R\Omega}{C^2} = \frac{4A\Omega}{C^2}. \tag{34}$$

Equation (32) is same as (34) in the vacuum. Corresponding phase difference is

$$\Delta\phi = \frac{2\pi\Delta t c}{\lambda} = \frac{8\pi A\Omega}{\lambda c}. \tag{35}$$

The difference in path length can be expressed as

$$\Delta L = 2R\Omega t = \frac{4\pi R^2 N}{c}\Omega, \tag{36}$$

and the corresponding phase difference between the two beams is

$$\Delta\phi = \frac{8\pi^2 R^2 N}{\lambda c}\Omega,$$
$$\Delta\phi_{Sagnac} = \frac{8\pi A}{c\lambda}\Omega, \quad A = \pi R^2. \tag{37}$$

It is interesting to note that although the above calculation is over-simplified (e.g., the speed of light in vacuum was assumed instead of that in the glass fiber), it yields the correct result. Exact relativistic calculations show that the phase shift is indeed independent of the material of the wave guide and the above equations apply.

Since the Sagnac effect was discovered, this theory is applied to manufacture the whole optical gyroscope such as laser gyroscope, ring gyroscope, fiber optical gyroscope, and so forth. The fiber optical gyroscope systems are hasty developed due to many advantages like no movement parts inside, high precision output, long consumption, and so forth.

The Sagnac effect method is based on two light beams path-length different created by rotation speed. The long distance light path is required because of the highlight speed. So the disadvantages of Sagnac effect gyroscope system are large in size and weight, complex fabrication processes due to long fiber optical or optical integrated chip.

As mentioned above, in MOEMS gyroscope the light phase shift created by rotation velocity is described

$$\Delta\phi_{MOEMS\_Gyro} = \frac{4\pi}{\lambda} l_0 + \frac{4\pi}{\lambda} \frac{2x_{max} Q_y}{\omega_y} \Omega \sin(\omega_d t). \tag{38}$$

Because $(4\pi/\lambda)l_0$ is constant number, which is defined by initialization interferometer cavity length,

$$\Delta\phi_{MOEMS\_Gyro} - \frac{4\pi}{\lambda} l_0 = \frac{8\pi}{\lambda} \frac{x_{max} Q_y}{\omega_y} \Omega \sin(\omega_d t). \tag{39}$$

Assume, at the same input rotation velocity for each gyroscope system, that two-phase shift ratios are

$$\frac{\Delta\phi_{MOEMS\_Gyro} - (4\pi/\lambda)l_0}{\Delta\phi_{Sagnac}} = \frac{8\pi}{\lambda} \frac{x_{max} Q_y}{\omega_y} \Omega \sin(\omega_d t) / \frac{8\pi A}{c\lambda}\Omega,$$
$$|\Delta\phi_{MOEMS\_Gyro}| = \left| \left(\frac{x_{max} Q_y}{\omega_y} \frac{c}{A} \right) \Delta\phi_{Sagnac} \right| + \frac{4\pi}{\lambda} l_0. \tag{40}$$

Here $(x_{max} Q_y/\omega_y)(c/A) \geq 1$, which means the sensitivity of MOEMS gyroscope system, is higher than optical gyroscope using Sagnac effect method. So the MOEMS gyroscope design is satisfied to civilization and military user.

5. CONCLUSION

In this paper, the combination of the micro-optical interferometer readout system and MEMS vibratory gyroscope is proposed. This novel micro-optical gyroscope has possessed microsize, light weight, and high performance features due to MEMS fabrication technology and the precision feature of the optical interferometer principle. According to comparison with Sagnac effect, the sensitivity and measurement range of this MOEMS gyroscope system are at the same level as the FOG system. The real-time testing results for the MOEMS gyroscope must wait for the first prototype coming out. The full performance comparisons between the MOEMS and FOG system will be investigated.

The novel optical MEMS gyroscope system is the perfect MOEMS application to combine the optical and MEMS technology. On the size aspect, the MEMS vibratory structure has been proved and fabricated to convert the rotation speed to the vibration movement due to Coriolis force theory. On the performance aspect, the microfiber optical interferometer has solved the precision distance readout comparing with the electrical readout. The novel optical MEMS gyroscope can be used from the rate grade to the inertial grade for the pose stability control in the missile, satellite, motion detector in the entertainment system like PC game, camera, or hard drive protector.

The operation principles of the MOEMS gyro system have been clearly discussed and created; the mathematics

model successfully includes the theory and equations. The MEMS fabrication processes and package for both the microvibration part and the micro-optical readout system will be discussed in the other paper. The first prototype has been sent to MEMS foundry after the software simulating.

ACKNOWLEDGMENT

The supports from South Africa National Research Foundation and AMSCOR are acknowledged.

REFERENCES

[1] N. Yazdi, F. Ayazi, and K. Najafi, "Micromachined inertial sensors," *Proceedings of the IEEE*, vol. 86, no. 8, pp. 1640–1658, 1998.

[2] F Ayazi and K. Najafi, "Design and fabrication of a high-performance polysilicon vibrating ring gyroscope," in *Proceedings of the 11th IEEE Annual International Workshop on Micro Electro Mechanical Systems (MEMS '98)*, pp. 621–626, Heidelberg, Germany, January 1998.

[3] D. Cho, S. Lee, and S. Park, "Surface/bulk micromachined high performance silicon micro-gyroscope," in *Proceedings of the Solid-State Sensor Actuator Workshop*, Hilton Head Island, SC, USA, June 2000.

[4] D. Kristiansen and O. Egeland, "Modeling of nonlinear vibrations for analysis and control of cylinder gyroscopes," in *Proceedings of the 37th IEEE Conference on Decision and Control (CDC '98)*, vol. 4, pp. 4326–4327, Tampa, Fla, USA, December 1998.

[5] T. Juneau, A. P. Pisano, and J. H. Smith, "Dual axis operation of a micromachined rate gyroscope," in *Proceedings of the International Conference on Solid-State Sensors and Actuators (Transducers '97)*, vol. 2, pp. 883–886, Chicago, Ill, USA, June 1997.

[6] J. Bernstein, S. Cho, A. T. King, A. Kourepenis, P. Maciel, and M. Weinberg, "A micromachined comb-drive tuning fork rate gyroscope," in *Proceedings of the IEEE Annual International Workshop on Micro Electro Mechanical Systems (MEMS '93)*, pp. 143–148, Fort Lauderdale, Fla, USA, February 1993.

[7] X. Jiang, J. I. Seeger, M. Kraft, and B. E. Boser, "A monolithic surface micromachined Z-axis gyroscope with digital output," in *Proceedings of IEEE Symposium on VLSI Circuits (VLSI '00)*, pp. 16–19, Honolulu, Hawaii, USA, June 2000.

[8] W. Ecke, P. Pfeifer, J. Schauer, R. Willsch, and K.-H. Jackel, "Fiber optic displacement measuring system for high-temperature seismic sensor," in *Fiber Optic and Laser Sensors XIV*, vol. 2839 of *Proceedings of SPIE*, pp. 290–301, Denver, Colo, USA, August 1996.

[9] "Fiber Optic Interferometer Fabry-Perot," http://www.physics.nad.ru/sensors/English/interf.htm.

[10] E. J. Eklund and A. M. Shkel, "Factors affecting the performance of micromachined sensors based on fabry-perot interferometry," *Journal of Micromechanics and Microengineering*, vol. 15, no. 9, pp. 1770–1776, 2005.

[11] E. Udd, "Fiber optic smart structures," *Proceedings of the IEEE*, vol. 84, no. 6, pp. 884–894, 1996.

[12] D. Hofstetter, H. P. Zappe, and R. Dandliker, "Optical displacement measurement with GaAsrAlGaAs-based monolithic integrated Michelson interferometers," *IEEE Journal of Lightwave Technology*, vol. 15, no. 4, pp. 663–670, 1997.

[13] H. Lefevre, "Principle of the fiber-optical gyroscope," in *The Fiber Optic Gyroscope*, chapter 2, pp. 5–72, Artech House, Boston, Mass, USA, 1993.

Hindawi Publishing Corporation
Journal of Nanomaterials
Volume 2008, Article ID 638523, 5 pages
doi:10.1155/2008/638523

Research Article

Fabrication and Characterization of ZnO Nanowire Arrays with an Investigation into Electrochemical Sensing Capabilities

Jessica Weber,[1,2] Sathyaharish Jeedigunta,[2,3] and Ashok Kumar[1,2]

[1] *Department of Mechanical Engineering, University of South Florida, Tampa, FL 33620, USA*
[2] *Nanomaterials and Nanomanufacturing Research Center, University of South Florida, Tampa, FL 33620, USA*
[3] *Department of Electrical Engineering, University of South Florida, Tampa, FL 33620, USA*

Correspondence should be addressed to Ashok Kumar, akumar@eng.usf.edu

Received 25 August 2008; Accepted 25 November 2008

Recommended by Rakesh Joshi

ZnO nanowire arrays were grown on a Si (100) substrate using the vapor-liquid-solid (VLS) method. ZnO nanowires were characterized by XRD, SEM, bright field TEM, and EDS. They were found to have a preferential orientation along the *c*-axis. The as-prepared sample was functionalized with glucose oxidase by physical adsorption. FTIR was taken before and after functionalization to verify the presence of the attached enzyme. Electrochemical measurements were performed on the nanowire array by differential pulse voltammetry in the range of −0.6 to 0.4 V. The nanoarray sensor displayed high sensitivity to glucose in the range of 1.0×10^{-4} to 1.0×10^{-2} mol L^{-1}.

1. INTRODUCTION

One-dimensional metal-oxide nanostructures have gained prominence after the immense interest developed in the synthesis of carbon nanotubes and its wide range of applications [1]. Metal oxides such as SnO_2 [2], TiO_2 [3], In_2O_3 [4], ITO [5], Ga_2O_3 [6], and ZnO [7] have been synthesized into nanowires, nanorods, nanobelts, and nanohelices. Due to their excellent electronic and optical properties, they are widely found in transparent electronic devices [8], flat panel displays [9], field emitters [10], electrochemical sensors, and toxic gas sensors [11]. As a biocompatible semiconducting material, ZnO is being actively investigated for biosensor applications [12–14].

Miniaturization is one ongoing important development in biosensor technology. Miniaturization, however, may result in low current because of the decreased amount of immobilized enzyme onto the available active area. It has already been reported that nanostructures can enhance the sensitivity of a biosensor by one to two orders of magnitude, due to the large surface area per unit volume ratio, which allows the immobilization of a larger amount of the enzyme. Since the development of the first glucose sensor enzyme electrode performance, stability and selectivity have been a main thrust for further research [15]. The incorporation of biomolecules into carbon nanotubes (CNTs) and metal oxide nanowires is achieved through various methods of immobilization such as covalent linkage [16], entrapment [17], cross-linking with glutaraldehyde [18], microencapsulation [19], and adsorption [20–22]. Adsorption is one of the more common schemes of immobilization because it is a method that requires minimal preparation. In this work, prolonged exposure of glucose oxidase to ZnO nanowires has resulted in enzyme immobilization through nonspecific adsorption of the enzyme on the sidewalls of the nanowires. This letter reports on the synthesis and characterization of ZnO nanowires by vapor-liquid-solid (VLS) mechanism and its application as an electrode for glucose measurement without any additional protective coating.

2. METHODS AND MATERIALS

For the growth of ZnO nanowires, ZnO nanopowder (99.999%, Sigma ~50–70 nm grain size) and graphite nanopowder (99.99%, Sigma ~70 nm) in 1 : 1 ratio were mixed to form a homogenous source weighing 300 mg. For the amperometric glucose detection, glucose oxidase (GOX, EC 1.1.3.4, type II from *Aspergillus niger*, 47 200 U/g),

D-(+)-glucose (purity 99.5%), and potassium phosphate were purchased from Sigma-Aldrich, St. Louis, Mo, USA. Phosphate buffer electrolyte solutions (PBSs) with various pHs were prepared from standard stock solutions of KH_2PO_4 and K_2HPO_4. All solutions were prepared with deionized water.

A high temperature furnace (Lindberg/Blue) was used for the growth of ZnO nanowires. As synthesized products were characterized by X-ray diffraction with Cu-Kα radiation (Philips X'pert Pro diffractometer), field emission scanning electron microscopy (FE-SEM, Hitachi S-800), and high-resolution transmission electron microscopy (FEI Tecnai F30, HR-TEM). TEM specimens were prepared by ultrasonicating the ZnO nanowires in methanol and dispersing a drop of solution on a carbon-coated copper grid. Chemical compositional analysis was carried out by EDX coupled with the HR-TEM system.

Electrochemical experiments were performed using a Princeton Applied Research PARSTAT 2263 advanced electrochemical analyzer. All electrochemical measurements were executed in a standard three-electrode system at room temperature. The modified zinc oxide sample acted as the working electrode, with an Ag/AgCl (3 M KCl) reference electrode, and a platinum wire (CH Instruments, Tex, USA) counter electrode. All potentials given in this paper are relative to the Ag/AgCl electrode. The pH of the glucose solutions was measured with a Fisher Scientific AB15 pH meter. FTIR studies were performed on a Perkin-Elmer Spectrum One FT-IR Spectrometer.

For the fabrication of a glucose sensor, we have initially grown an array of ZnO nanowires on Si (100) via thermal evaporation, with the use of a gold catalyst. Freshly prepared ZnO source powder and substrates were loaded in two different alumina boats in the high-temperature and low-temperature zones of the vacuum furnace, respectively. The furnace was initially evacuated to a pressure of 10^{-3} Torr and argon was then passed at a constant flow rate of 500 sccm. The temperature of the furnace was approximately raised to 900°C–950°C. The substrates were unloaded after the furnace was cooled to room temperature. The zinc oxide nanowire array was then functionalized with the enzyme glucose oxidase. Approximately 15 IU of GOX was applied onto the nanowire surface via physical adsorption. The newly constructed electrode was allowed to dry over 24 hours at room temperature prior to use.

3. RESULTS AND DISCUSSION

The X-ray diffraction pattern of the as-grown ZnO products is shown in Figure 1. All the visible peaks are indexed to a wurtzite (hexagonal) structure of ZnO with lattice constants of $a = 0.3250$ nm and $c = 0.5205$ nm, respectively [23]. A small shift was observed in the peaks of ZnO nanowires when compared to ZnO bulk. This might be due to the thermal stresses developed at the time of growth. In addition, Au (111) and Au (200) peaks were also detected from the XRD pattern. The high intensity of (002) peak of ZnO nanowires shows that the preferential growth direction is along the *c*-axis.

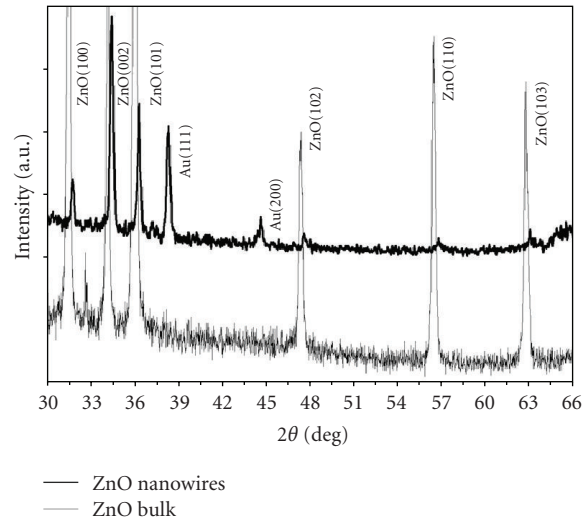

Figure 1: (upper curve) X-ray diffraction spectrum of an array of ZnO nanotubular structures and (lower curve) bulk ZnO, respectively.

The surface morphology of the patterned sample can be observed in the SEM images (see Figure 2). The ZnO nanowires have a typical length of 0.5–2 μm and a diameter of 40–120 nm. Figure 3 shows the TEM image of a pair of nanowires and inset shows the electron diffraction pattern of the wires. It is clearly shown from the electron diffraction pattern that the one-dimensional nanowires were single crystal and grown along [0001]. A representative energy dispersive X-ray (EDX) spectrum was performed near the tip of the ZnO nanowire as indicated by the arrow shown in Figure 3(c). The peaks associated with Zn, O, Au, Cu, and C are seen in the EDX spectrum, where the peak corresponding to Au confirms that the tips of the nanowires were encapsulated with a gold particle of diameter ~52 nm (see Figure 3(c)) and the copper and carbon signatures are from the carbon-coated copper TEM grid.

The as-grown ZnO nanowires on silicon substrate were analyzed by Fourier transform infrared (FTIR) spectroscopy before and after functionalization with GOX (see Figure 4). The absorption peak at about 1000 cm^{-1} can be interpreted as the Si-O-Zn vibrational mode [24]. GOX is seen through the presence of the primary amine group. The N-H bending is observed at 1600 cm^{-1} while the N-H stretch due to asymmetric and symmetric vibrations occurs at 3400 cm^{-1} and 3300 cm^{-1}, respectively. The activity of the enzyme glucose oxidase is affected by the pH of the glucose solution. The pH dependence of the sensor was evaluated at 5 mM glucose solutions in the range of pH 6 to 9 (see Figure 5). An optimal peak current of the sensor was displayed at pH 6.5. Considering that the pH of human blood is about 7.4, the amperometric experiments were performed at pH 7.0. Figure 6 shows the cyclic voltammograms of the ZnO-GOX electrode in PBS at a pH of 7.0 and at room temperature. The inset shows the plot of peak current versus the square root of the scan rate. The plot is nearly linear with less than 3% error from 50 to 400 mV s^{-1}. The decrease in current response

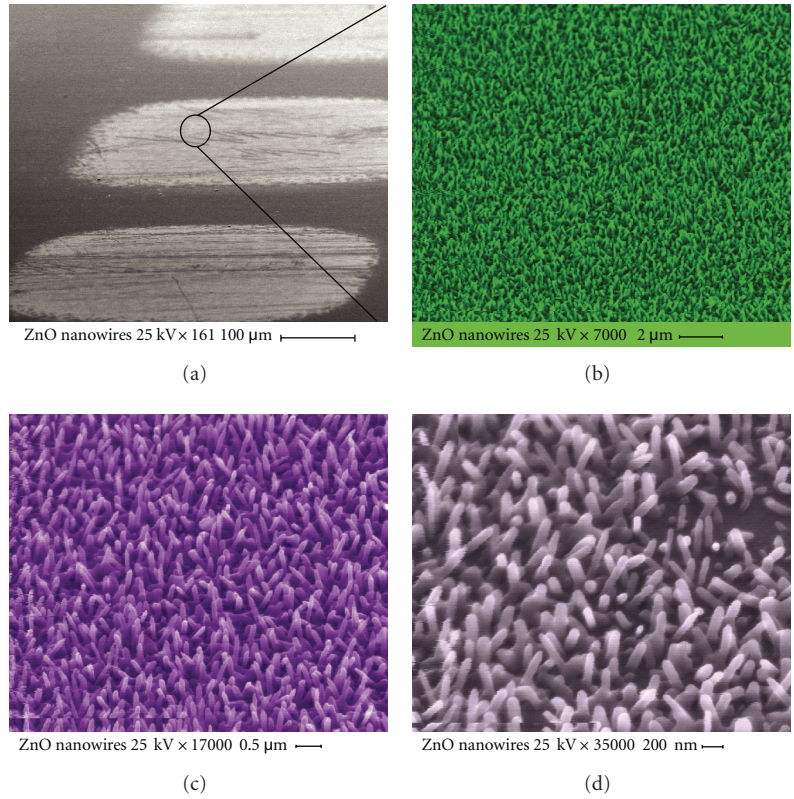

Figure 2: (a) Low magnification top-view SEM image of patterned ZnO nanotubes. (b–d) Side view of patterned- and aligned-ZnO nanotubes from lower to higher magnification (clockwise direction).

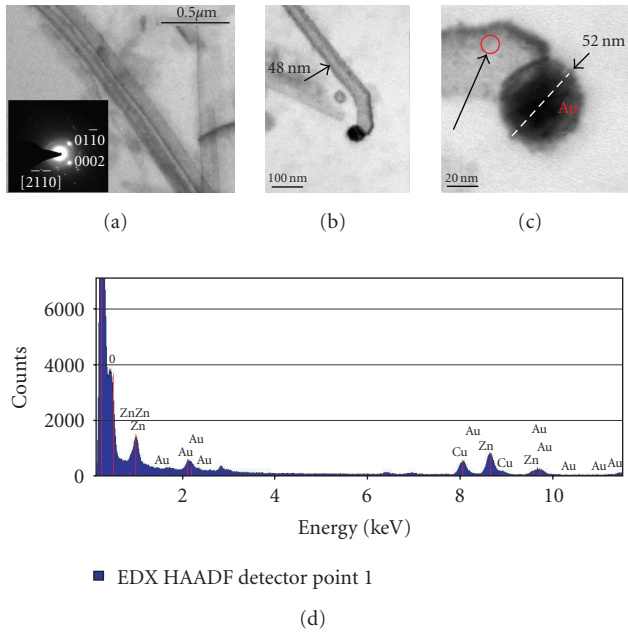

Figure 3: (a) Bright field TEM image of a pair of ZnO nanotubes, inset shows electron diffraction pattern on a pair of ZnO nanotubes along the zone axis [2 $\bar{1}\bar{1}$ 0]. (b) TEM image of a ZnO nanotube with an Au particle at the end. (c) Shows high-resolution image of the end of the ZnO nanotube. (d) EDS spectrum recorded near the catalyst particle indicated by arrow.

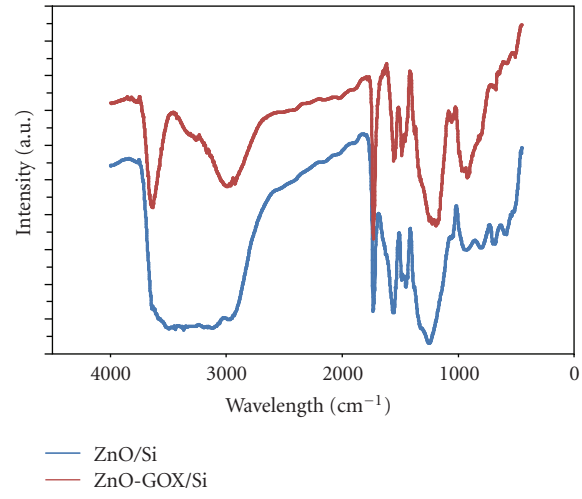

Figure 4: FTIR spectra of (lower curve) ZnO nanowires and (upper curve) glucose oxidase entrapped-ZnO nanowires, onto Si substrate.

with successive increase in scan rate indicates that the electrode reaction is diffusion controlled. The direct pulse voltammetry (DPV) response of the sensor to successive increments of glucose is shown in Figure 7(a). These results were obtained with a scan rate of 0.020 mV/s, step height

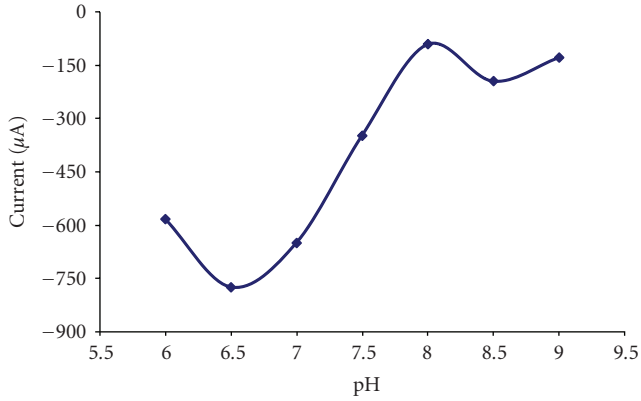

Figure 5: Current response of ZnO-based glucose sensor in PBS with increasing pH containing 5.0×10^{-3} mol L^{-1} glucose.

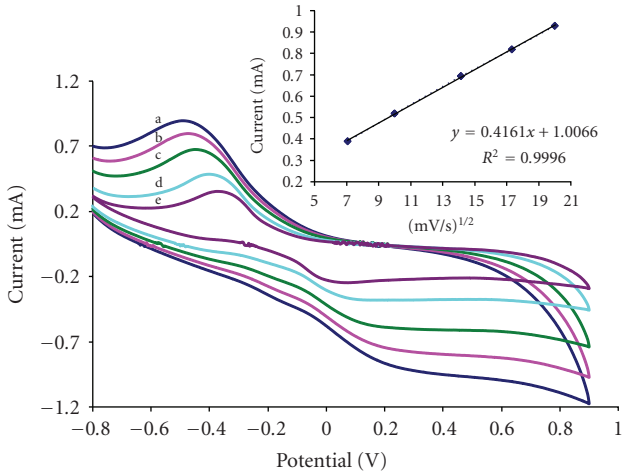

Figure 6: Cyclic voltammograms of ZnO-GOX/Si in PBS (pH 7.0) containing 5.0×10^{-3} mol L^{-1} glucose at a scan rate of (a) 50 mV s^{-1}, (b) 100 mV s^{-1}, (c) 200 mV s^{-1}, (d) 300 mV s^{-1}, and (e) 400 mV s^{-1}. Inset plot: relationship between scan rate and response current of ZnO-GOX/Si in PBS (pH 7.0) containing 5.0×10^{-3} mol L^{-1} glucose.

of 2 mV, and a potential sweep between −0.6 and 0.4 V. The well-defined peaks occur at approximately −0.05 V, showing that the enzyme is active at this potential. This data displays a linear relationship of current to the corresponding glucose concentration. The calibration response curve (see Figure 7(b)) shows a linear trend in the range of 1.0×10^{-4} to 1.0×10^{-2} mol L^{-1} glucose with an r-value of 0.9903 and less than 5% error.

4. CONCLUSIONS

The successful fabrication of a highly selective ZnO nanowire-based amperometric glucose biosensor has been achieved. The ZnO electrodes were synthesized on Si (100) substrates by VLS mechanism. High-density ZnO nanowires with a large surface area are found to have a preferential growth direction along [0001] axis. No additional protective coating has been utilized during the electrode preparation.

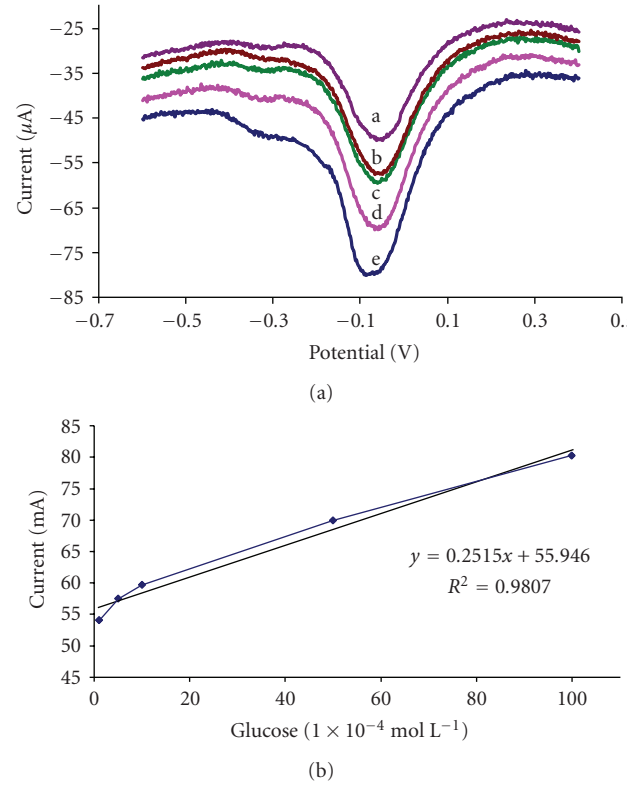

Figure 7: (a) DPV response of ZnO-GOX/Si in PBS (pH 7.0) at (a) 1×10^{-4} mol L^{-1}, (b) 5×10^{-4} mol L^{-1}, (c) 1×10^{-3} mol L^{-1}, (d) 5×10^{-3} mol L^{-1}, and (e) 1×10^{-2} mol L^{-1} glucose. (b) Linear calibration curve of ZnO-GOX biosensor.

The sensor functioned in the range of 1.0×10^{-4} to 1.0×10^{-2} mol L^{-1} glucose. The biosafe nature of ZnO and successful immobilization of glucose oxidase onto the electrode surface leads to a new novel approach to biosensor construction and applications.

ACKNOWLEDGMENTS

The authors would like to acknowledge the generous support of the National Science Foundation. This research was supported by the following National Science Foundation (NSF) grants: NIRT no. 0404137, Crest no. 0734232, IGERT no. 0221681, and GK12 no. 0638709.

REFERENCES

[1] N. Hamada, S.-I. Sawada, and A. Oshiyama, "New one-dimensional conductors: graphitic microtubules," *Physical Review Letters*, vol. 68, no. 10, pp. 1579–1581, 1992.

[2] J. Zhang, F. Jiang, and L. Zhang, "Synthesis of SnO_2 nanobelts and their structural characterization," *Journal of Physics D*, vol. 36, no. 2, pp. L21–L24, 2003.

[3] B. Xiang, Y. Zhang, Z. Wang, et al., "Field-emission properties of TiO_2 nanowire arrays," *Journal of Physics D*, vol. 38, no. 8, pp. 1152–1155, 2005.

[4] C. Li, D. Zhang, X. Liu, et al., "In_2O_3 nanowires as chemical sensors," *Applied Physics Letters*, vol. 82, no. 10, pp. 1613–1615, 2003.

[5] D. Yu, D. Wang, W. Yu, and Y. Qian, "Synthesis of ITO nanowires and nanorods with corundum structure by a co-precipitation-anneal method," *Materials Letters*, vol. 58, no. 1-2, pp. 84–87, 2004.

[6] K.-W. Chang and J.-J. Wu, "Formation of β-Ga_2O_3-TiO_2 'nanobarcodes' from core-shell nanowires," *Advanced Materials*, vol. 17, no. 2, pp. 241–245, 2005.

[7] D. Banerjee, J. Rybczynski, J. Y. Huang, D. Z. Wang, K. Kempa, and Z. F. Ren, "Large hexagonal arrays of aligned ZnO nanorods," *Applied Physics A*, vol. 80, no. 4, pp. 749–752, 2005.

[8] J. P. Santos and J. A. de Agapito, "The interaction of oxygen with nanocrystalline SnO_2 thin films in the framework of the electron theory of adsorption," *Thin Solid Films*, vol. 338, no. 1-2, pp. 276–280, 1999.

[9] T. Mahalingam, V. S. John, M. Raja, Y. K. Su, and P. J. Sebastian, "Electrodeposition and characterization of transparent ZnO thin films," *Solar Energy Materials and Solar Cells*, vol. 88, no. 2, pp. 227–235, 2005.

[10] C. J. Lee, T. J. Lee, S. C. Lyu, Y. Zhang, H. Ruh, and H. J. Lee, "Field emission from well-aligned zinc oxide nanowires grown at low temperature," *Applied Physics Letters*, vol. 81, no. 19, p. 3648, 2002.

[11] J. Ding, T. J. McAvoy, R. E. Cavicchi, and S. Semancik, "Surface state trapping models for SnO_2-based microhotplate sensors," *Sensors and Actuators B*, vol. 77, no. 3, pp. 597–613, 2001.

[12] Q. Wan, Q. H. Li, Y. J. Chen, et al., "Fabrication and ethanol sensing characteristics of ZnO nanowire gas sensors," *Applied Physics Letters*, vol. 84, no. 18, pp. 3654–3656, 2004.

[13] B. S. Kang, F. Ren, Y. W. Heo, L. C. Tien, D. P. Norton, and S. J. Pearton, "*p*H measurements with single ZnO nanorods integrated with a microchannel," *Applied Physics Letters*, vol. 86, no. 11, Article ID 112105, 3 pages, 2005.

[14] F. Zhang, X. Wang, S. Ai, et al., "Immobilization of uricase on ZnO nanorods for a reagentless uric acid biosensor," *Analytica Chimica Acta*, vol. 519, no. 2, pp. 155–160, 2004.

[15] L. C. Clark and C. Lyons, "Electrode systems for continuous monitoring in cardiovascular surgery," *Annals of the New York Academy of Sciences*, vol. 102, pp. 29–45, 1962.

[16] M. A. Rahman, D.-S. Park, and Y.-B. Shim, "A performance comparison of choline biosensors: anodic or cathodic detections of H_2O_2 generated by enzyme immobilized on a conducting polymer," *Biosensors and Bioelectronics*, vol. 19, no. 12, pp. 1565–1571, 2004.

[17] J. C. Vidal, E. Garcia-Ruiz, J. Espuelas, T. Aramendia, and J. R. Castillo, "Comparison of biosensors based on entrapment of cholesterol oxidase and cholesterol esterase in electropolymerized films of polypyrrole and diaminonaphthalene derivatives for amperometric determination of cholesterol," *Analytical and Bioanalytical Chemistry*, vol. 377, no. 2, pp. 273–280, 2003.

[18] J.-J. Xu, D.-M. Zhou, and H.-Y. Chen, "A reagentless hydrogen peroxide biosensor based on the coimmobilization of thionine and horseradish peroxidase by their cross-linking with glutaraldehyde on glassy carbon electrode," *Electroanalysis*, vol. 10, no. 10, pp. 713–716, 1998.

[19] D. Trau and R. Renneberg, "Encapsulation of glucose oxidase microparticles within a nanoscale layer-by-layer film: immobilization and biosensor applications," *Biosensors and Bioelectronics*, vol. 18, no. 12, pp. 1491–1499, 2003.

[20] R. J. Chen, Y. Zhang, D. Wang, and H. Dai, "Noncovalent sidewall functionalization of single-walled carbon nanotubes for protein immobilization," *Journal of the American Chemical Society*, vol. 123, no. 16, pp. 3838–3839, 2001.

[21] R. F. Lane and A. T. Hubbard, "Electrochemistry of chemisorbed molecules—I. Reactants connected to electrodes through olefinic substituents," *Journal of Physical Chemistry*, vol. 77, no. 11, pp. 1401–1410, 1973.

[22] R. F. Lane and A. T. Hubbard, "Electrochemistry of chemisorbed molecules—II. Influence of charged chemisorbed molecules on the electrode reactions of platinum complexes," *Journal of Physical Chemistry*, vol. 77, no. 11, pp. 1411–1421, 1973.

[23] K. Park, J.-S. Lee, M.-Y. Sung, and S. Kim, "Structural and optical properties of ZNO nanowires synthesized from ball-milled ZNO powders," *Japanese Journal of Applied Physics Part 1*, vol. 41, no. 12, pp. 7317–7321, 2002.

[24] J. P. Rainho, J. Rocha, L. D. Carlos, and R. M. Almeida, "^{29}Si nuclear-magnetic-resonance and vibrational spectroscopy studies of SiO_2-TiO_2 powders prepared by the sol-gel process," *Journal of Materials Research*, vol. 16, no. 8, pp. 2369–2376, 2001.

Hindawi Publishing Corporation
Journal of Nanomaterials
Volume 2008, Article ID 950967, 9 pages
doi:10.1155/2008/950967

Review Article

Nanomaterials for Hydrogen Storage Applications: A Review

Michael U. Niemann,[1] Sesha S. Srinivasan,[1] Ayala R. Phani,[2] Ashok Kumar,[1] D. Yogi Goswami,[1] and Elias K. Stefanakos[1]

[1] *Clean Energy Research Center, College of Engineering, University of South Florida, 4202 East Fowler Avenue, Tampa, FL 33620, USA*
[2] *Nano-RAM Technologies, 98/2A Anjanadri, 3rd Main, Vijayanagar, Bangalore 5600040, Karnataka, India*

Correspondence should be addressed to Sesha S. Srinivasan, sesha@eng.usf.edu

Received 21 June 2008; Accepted 21 September 2008

Recommended by Rakesh Joshi

Nanomaterials have attracted great interest in recent years because of the unusual mechanical, electrical, electronic, optical, magnetic and surface properties. The high surface/volume ratio of these materials has significant implications with respect to energy storage. Both the high surface area and the opportunity for nanomaterial consolidation are key attributes of this new class of materials for hydrogen storage devices. Nanostructured systems including carbon nanotubes, nano-magnesium based hydrides, complex hydride/carbon nanocomposites, boron nitride nanotubes, TiS_2/MoS_2 nanotubes, alanates, polymer nanocomposites, and metal organic frameworks are considered to be potential candidates for storing large quantities of hydrogen. Recent investigations have shown that nanoscale materials may offer advantages if certain physical and chemical effects related to the nanoscale can be used efficiently. The present review focuses the application of nanostructured materials for storing atomic or molecular hydrogen. The synergistic effects of nanocrystalinity and nanocatalyst doping on the metal or complex hydrides for improving the thermodynamics and hydrogen reaction kinetics are discussed. In addition, various carbonaceous nanomaterials and novel sorbent systems (e.g. carbon nanotubes, fullerenes, nanofibers, polyaniline nanospheres and metal organic frameworks etc.) and their hydrogen storage characteristics are outlined.

1. INTRODUCTION

The increase in threats from global warming due to the consumption of fossil fuels requires our planet to adopt new strategies to harness the inexhaustible sources of energy [1, 2]. Hydrogen is an energy carrier which holds tremendous promise as a new renewable and clean energy option [3]. Hydrogen is a convenient, safe, versatile fuel source that can be easily converted to a desired form of energy without releasing harmful emissions. Hydrogen is the ideal fuel for the future since it significantly reduces the greenhouse gas emissions, reduces the global dependence on fossil fuels, and increases the efficiency of the energy conversion process for both internal combustion engines and proton exchange membrane fuel cells [4, 5]. Hydrogen used in the fuel cell directly converts the chemical energy of hydrogen into water, electricity, and heat [6] as represented by

$$H_2 + \frac{1}{2}O_2 \longrightarrow H_2O + \text{Electricity} + \text{Heat}. \quad (1)$$

Hydrogen storage cuts across both hydrogen production and hydrogen applications and thus assumes a critical role in initiating a hydrogen economy [7–10]. For catering today's fuel cell cars, the onboard hydrogen storage is inevitable and an integral part of the system to be reengineered [11, 12]. The critical properties of the hydrogen storage materials to be evaluated for automotive applications are (i) light weight, (ii) cost and availability, (iii) high volumetric and gravimetric density of hydrogen, (iv) fast kinetics, (v) ease of activation, (vi) low temperature of dissociation or decomposition, (vii) appropriate thermodynamic properties, (viii) long-term cycling stability, and (ix) high degree of reversibility. All the said properties greatly demand from us to understand the fundamental mechanistic behavior of materials involving catalysts and their physicochemical reaction toward hydrogen at an atomic or molecular scale.

Various hydrogen storage systems (see Figure 1), such as metal hydrides, complex hydrides, chemical hydrides, adsorbents and nanomaterials (nanotubes, nanofibers,

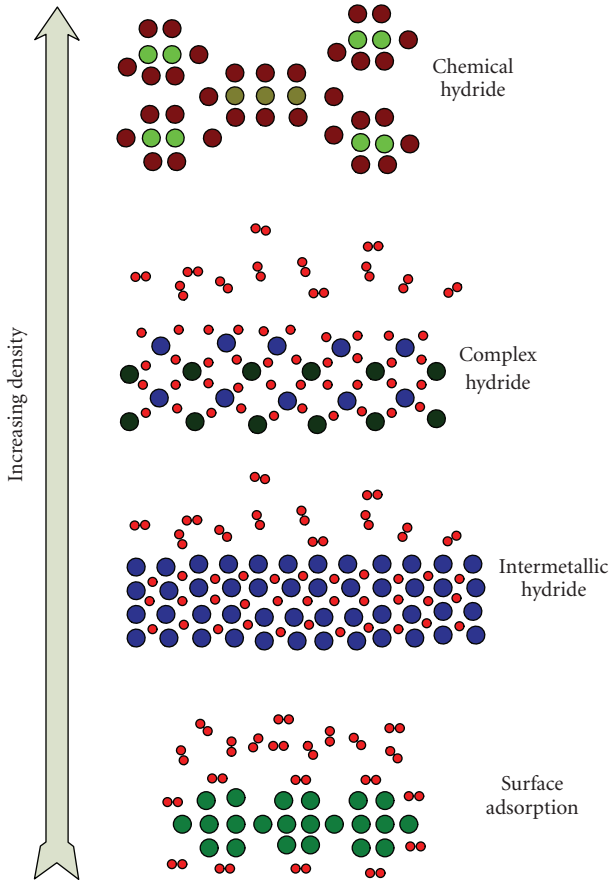

Figure 1: Hydrogen storage density in physisorbed materials, metal/complex, and chemical hydrides.

nanohorns, nanospheres, and nanoparticles), clathrate hydrates, polymer nanocomposites, metal organic frameworks, and so on [13–19], have been explored for onboard hydrogen storage applications. However, none of these materials qualifies and fulfill all hydrogen storage criteria such as (1) high hydrogen content (>6.0 wt.%), (2) favorable or tuning thermodynamics (30–55 kJ/mol H_2) (3) operate below 100°C for H_2 delivery, (4) onboard refueling option for a hydrogen-based infrastructure, (5) cyclic reversibility (~1000 cycles) at moderate temperatures, and so on. Among the various hydrogen storage systems, the concept of nanomaterials and their wide applications for energy storage [20] are discussed in the present paper.

2. NANOSTRUCTURED MATERIALS

Nanostructured materials have potential promise in hydrogen storage because of their unique features such as adsorption on the surface, inter- and intragrain boundaries, and bulk absorption [21, 22]. Nanostructured and nanoscale materials strongly influence the thermodynamics and kinetics of hydrogen absorption and dissociation by increasing the diffusion rate as well as by decreasing the required diffusion length. Additionally, the materials at the nanoscale offer the possibility of controlling material tailoring parameters

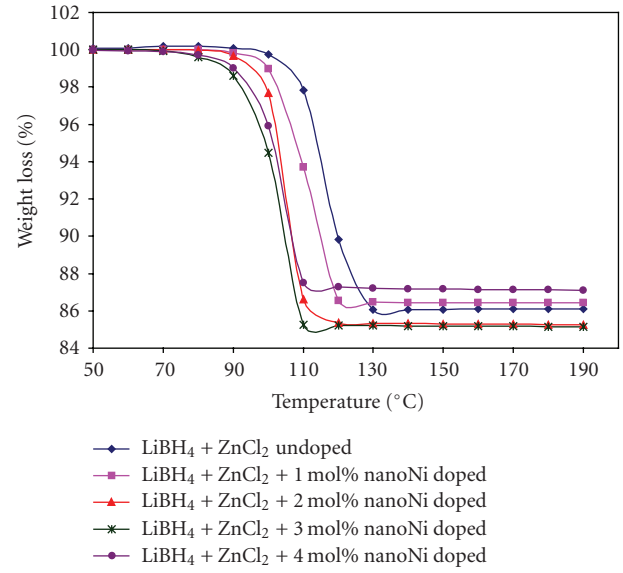

Figure 2: TGA curves for the $LiBH_4 + 1/2\ ZnCl_2$ undoped and Xmol% nano-Ni doped system ($X = 1, 2, 3, 4$).

independently of their bulk counterparts. They also lead to the design of light weight hydrogen storage systems with better hydrogen storage characteristics.

2.1. Nanocatalyst doping in complex borohydrides

Advanced complex hydrides that are light weight, low cost, and have high-hydrogen density are essential for onboard vehicular storage [8, 23, 24]. Some of the complex hydrides with reversible capacities achieved are Alanates [25, 26], Amides [27, 28], Borohydrides [29–31], and combinations thereof [32, 33]. The challenging tasks to design and develop the complex hydrides mandate an optimization and overcoming of kinetic and thermodynamic limitations [18, 34]. The enhancement of reaction kinetics at low temperatures and the requirement for high hydrogen storage capacity (>6.0 wt%) of hydrogen storage materials could be made possible by catalytic doping. If nanostructured materials with high surface area are used as the catalytic dopants, they may offer several advantages for the physicochemical reactions, such as surface interactions, adsorption in addition to bulk absorption, rapid kinetics, low-temperature sorption, hydrogen atom dissociation, and molecular diffusion via the surface catalyst. The intrinsically large surface areas and unique adsorbing properties of nanophase catalysts can assist the dissociation of gaseous hydrogen and the small volume of individual nanoparticles can produce short diffusion paths to the materials' interiors. The use of nanosized dopants enables a higher dispersion of the catalytically active species [35] and thus facilitates higher mass transfer reactions.

Figure 2 depicts the thermogravimetric weight loss profiles of the new complex borohydride ($LiBH_4 + 1/2\ ZnCl_2$) system undoped and doped with different nanocatalyst (e.g., nano-Ni) concentrations.

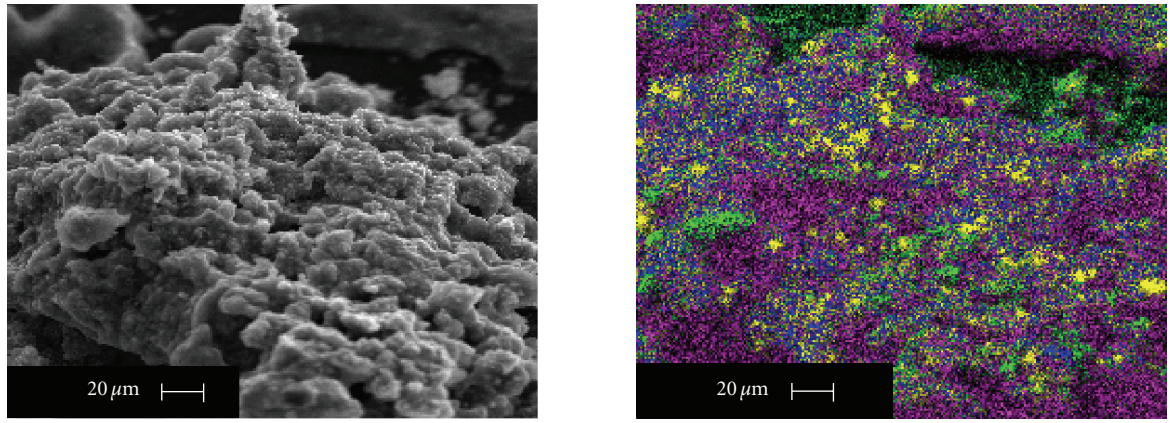

FIGURE 3: (a) SEM imaging and (b) EDS mapping of the sample $LiBH_4$ + 1/2 $ZnCl_2$ + 10 mol% nano-Ni (mapping elements—green: oxygen, yellow: nano-Ni, blue: chlorine, purple: zinc).

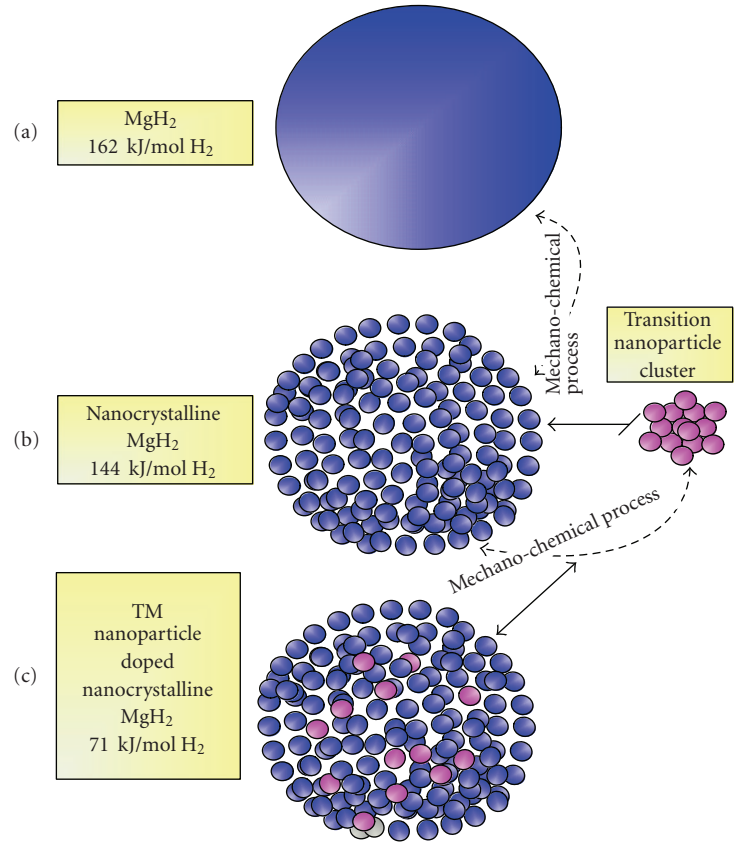

FIGURE 4: Conceptual model of MgH_2 cluster (a) plain, (b) nanocrystalline, and (c) nanocatalyst-doped materials.

The $Zn(BH_4)_2$, as obtained from the mechanochemical reaction of ($LiBH_4$ + 1/2 $ZnCl_2$), exhibits an endothermic melting transition at around 80–90°C (DSC signals are not shown in the figure) and a clear-cut weight loss occurs due to the thermal hydrogen decomposition at around 120°C. Trial experiments were conducted by introducing different nanocatalyst (nano-Ni (particle size of 3–10 nm) obtained from QuantumSphere Inc., Calif, USA) concentrations (X = 1, 2, 3, 4 mol%) in this complex system. It is clearly discernible from this figure that nanocatalyst doping helps to lower the temperature of decomposition from 120°C down to 100°C. A concentration of 3 mol% nano-Ni was found to

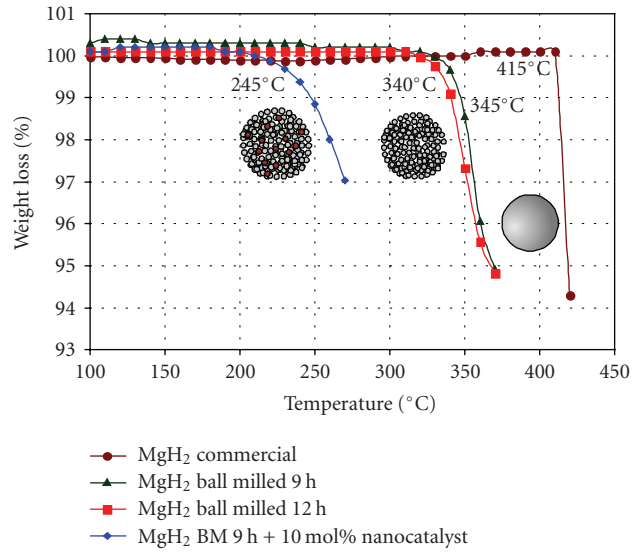

Figure 5: TGA curves for the (a) commercial; (b) micro-/nanocrystalline, and (c) 10 mol% nanocatalyst-doped nanocrystalline MgH_2.

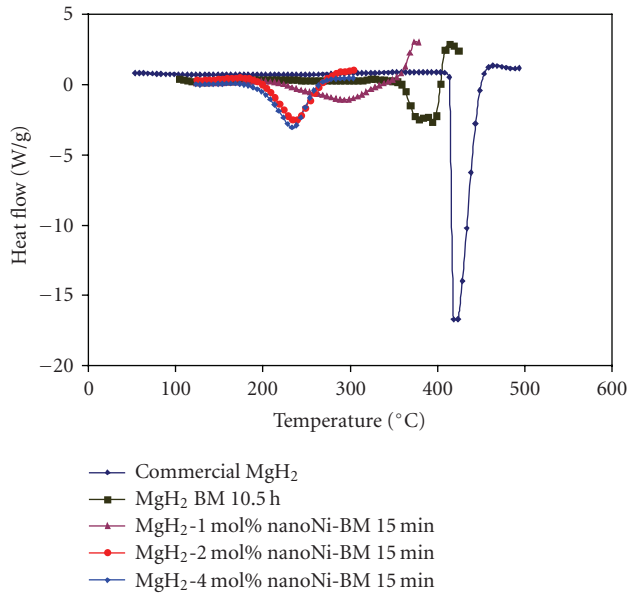

Figure 6: DSC profiles of (a) commercial, (b) ball milled for 10.5 hours, and (c) 10 mol% nano-Ni-doped nanocrystalline MgH_2.

be optimum for the gravimetric weight loss due to thermal decomposition at low temperature. It is also confirmed from the gravimetric analysis that nanocatalyst doping enhances the hydrogen storage characteristics such as reaction kinetics at low-decomposition temperatures (T_{dec}). The microstructures of the nanocatalyst doped complex hydride both in imaging mode and EDS mapping (distribution of different elements) mode as obtained from SEM are shown in Figures 3(a) and 3(b).

2.2. *Synergistic behavior of nanocatalyst doping and nanocrystalline form of MgH_2*

It is generally known that pristine MgH_2 theoretically can store ~7.6 wt.% hydrogen [36]. However, so far, magnesium hydride-based materials have limited practical applications because both hydrogenation and dehydrogenation reactions are very slow and, hence, relatively high temperatures are required [23]. Magnesium hydride forms ternary and quaternary hydride structures by reacting with various transition metals (Fe, Co, Ni, etc.) and thus improved kinetics. Moreover, the nanoscale version of these transition metal particles offers an additional hydrogen sorption mechanism via its active surface sites [36, 37]. In a similar way, the synergistic approach of doping nanoparticles of Fe and Ti with a few mol% of carbon nanotubes (CNTs) on the sorption behavior of MgH_2 has recently been investigated [38]. The addition of CNT significantly promotes hydrogen diffusion in the host metal lattice of MgH_2 due to the short pathway length and creation of fast diffusion channels [39]. The dramatic enhancement of kinetics of MgH_2 has also been explored through reaction with small amounts of $LiBH_4$ [40]. Though the MgH_2 admixing increases the equilibrium plateau pressure of $LiNH_2$ [41] or $LiBH_4$ [29], catalytic doping of these complex hydrides has not yet been investigated.It is generally believed that the role of the CNT/nanocatalyst on either $NaAlH_4$ or MgH_2 is to stabilize the structure and facilitate a reversible hydrogen storage behavior.

The phenomenon of mechanical milling helps to pulverize the particles of MgH_2 into micro- or nanocrystalline phases and thus leads to lowering the activation energy of desorption [42]. The height of the activation energy barrier depends on the surface elements. Without using the catalysts, the activation energy of absorption corresponds to the activation barrier for the dissociation of the H_2 molecule and the formation of hydrogen atoms. The activation energies of the H_2 sorption for the bulk MgH_2, mechanically milled MgH_2 and nanocatalyst-doped MgH_2, are shown in Figures 4(a) and 4(c).

It is undoubtedly seen that the activation barrier has been drastically lowered by nanocatalyst doping which suggests that the collision frequency between the H_2 molecules and transition metal nanoparticles increases with decreasing size of the catalyst. In addition, Figure 4 shows the conceptual model of an MgH_2 nanocluster and the distribution of nanocatalyst over the active surface sites for efficient hydrogen storage.

Recently, we have attempted to establish the above "proof of concept." Commercial MgH_2 exhibits weight loss due to hydrogen decomposition at higher temperature (e.g., 415°C) (see Figure 5).

However, the mechanochemical milling of MgH_2 introduces defects and particle size reduction. Thus, obtained micro-/nanocrystalline MgH_2 grains show endothermic hydrogen decomposition (see Figure 6) at an earlier temperature of 340°C. In addition, to nanoscale formation, the doping by a nanocatalyst certainly decreases the onset transition temperature by as much as 100°C (Figures 5 and 6).

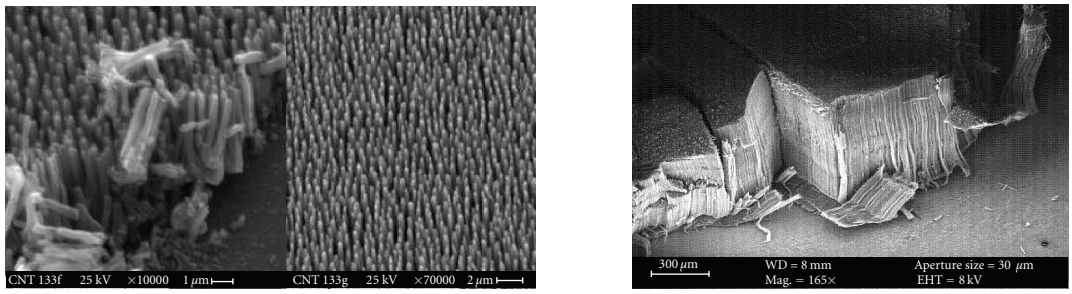

(a) (b)

Figure 7: SEM micrographs of (a) carbon nanotubes grown by MPECVD and (b) high density of aligned carbon nanotubes.

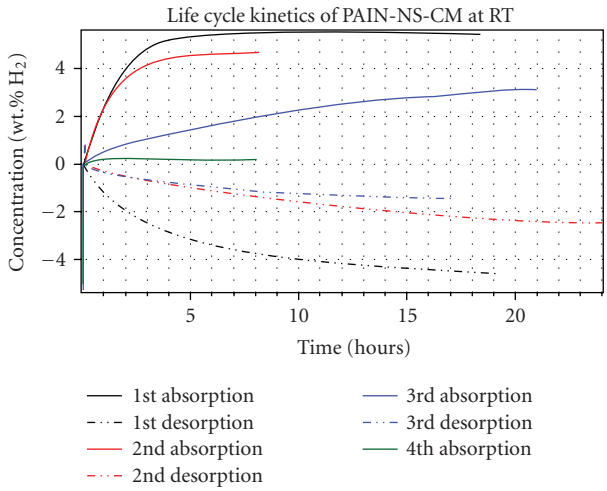

Figure 8: Hydrogen sorption kinetics of polyaniline nanospheres at room temperature showing good reversibility in the initial runs.

2.3. *Carbonaceous nanomaterials (carbon nanotubes, fullerenes, and nanofibers)*

Carbonaceous materials are attractive candidates for hydrogen storage because of a combination of adsorption ability, high specific surface area, pore microstructure, and low-mass density. In spite of extensive results available on hydrogen uptake by carbonaceous materials, the actual mechanism of storage still remains a mystery. The interaction may either be based on van der Walls attractive forces (physisorption) or on the overlap of the highest occupied molecular orbital of carbon with occupied electronic wave function of the hydrogen electron, overcoming the activation energy barrier for hydrogen dissociation (chemisorption). The physisorption of hydrogen limits the hydrogen-to-carbon ratio to less than one hydrogen atom per two carbon atoms (i.e., 4.2 mass %). While in chemisorption, the ratio of two hydrogen atoms per one carbon atom is realized as in the case of polyethylene [43–45]. Physisorbed hydrogen has a binding energy normally of the order of 0.1 eV, while chemisorbed hydrogen has C–H covalent bonding, with a binding energy of more than 2-3 eV.

Dillon et al. presented the first report on hydrogen storage in carbon nanotubes [46] and triggered a worldwide tide of research on carbonaceous materials. Hydrogen can be physically adsorbed on activated carbon and be "packed" on the surface and inside the carbon structure more densely than if it has just been compressed. The best results achieved with carbon nanotubes to date confirmed by the National Renewable Energy Laboratory are hydrogen storage density corresponding to about 10% of the nanotube weight [47].

In the present study, carbon nanotubes have been successfully grown by microwave plasma-enhanced chemical vapor deposition (MPECVD), a well-established method [46, 47]. Figure 7(a) represents the as-grown carbon nanotubes on a substrate using optimized processing conditions such as temperature, gas flow, gas concentrations, and pressure. Aligned nanotubes, as seen in Figure 7(b), have been grown to ensure uniformity in the nanotubes' dimensions. Various seed materials have been investigated to grow carbon nanotubes and attempted to determine any effect on the hydrogen sorption capacities.

Fullerenes, on the other hand, a new form of carbon with close-caged molecular structure were first reported by Kroto et al. in 1985 [48]. It is a potential hydrogen storage material based on the ability to react with hydrogen via hydrogenation of carbon-carbon double bonds. The theory predicts that a maximum of 60 hydrogen atoms can be attached to both the inside (endohedrally) and outside (exohedrally) of the fullerene spherical surface. Thus, a stable $C_{60}H_{60}$ isomer can be formed with the theoretical hydrogen content of ~7.7 wt%. It seems that the fullerene hydride reaction is reversible at high temperatures. The 100% conversion of $C_{60}H_{60}$ indicates that 30 moles of H_2 gas will be released from each mole of fullerene hydride compound. However, this reaction is not possible because it requires high temperature, about 823–873 K [49]. Solid C_{60} has face-centered cubic lattice at room temperature and its density is ~1.69 g/sm^3. Molecules are freely rotating due to weak intermolecular interaction. Fullerene is an allotropic modification of carbon. Fullerene molecules are composed of pentagons and hexagons whose vertexes contain carbon atoms. Fullerene, C_{60}, is the smallest and the most stable structure (owing to high degree of its symmetry).

Hydrogen can be stored in glass microspheres of approximately 50 μm diameter. The microspheres can be filled with

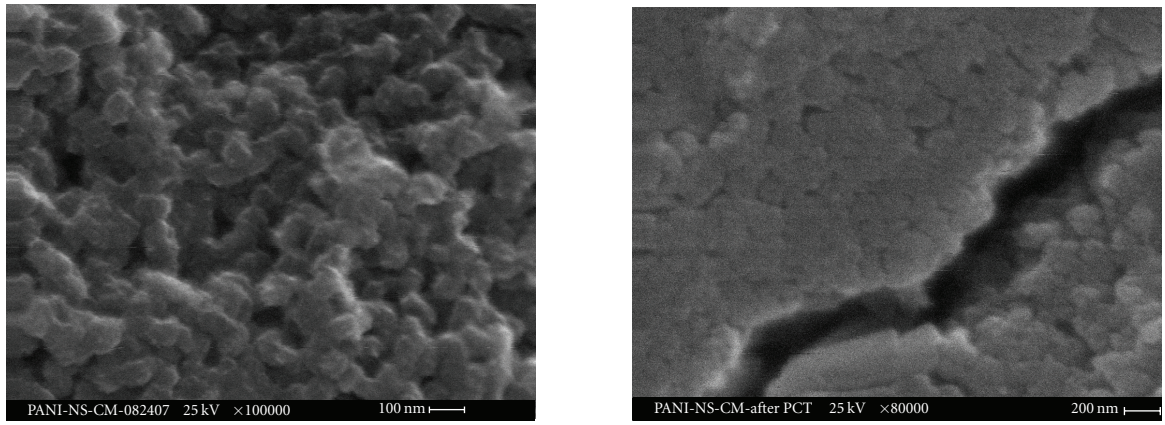

(a) (b)

Figure 9: SEM images of polyaniline nanospheres (a) as-prepared and (b) after hydrogen sorption cycles.

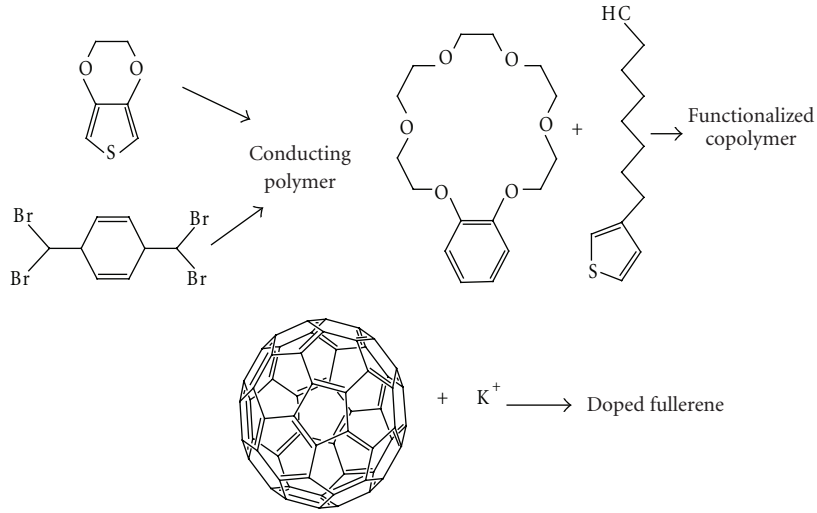

Figure 10: Schematics for the development of functionalized conducting polymer.

hydrogen by heating them to increase the glass permeability to hydrogen. At room temperature, a pressure of approximately 25 MPa is achieved resulting in storage density of 14% mass fraction and 10 kg H_2/m^3 [49]. At 62 MPa, a bed of glass microspheres can store 20 kg H_2/m^3. The release of hydrogen occurs by reheating the spheres to again increase the permeability.

2.4. Nanocomposite conducting polymers

Nanocomposite material consisting of a polyaniline matrix, which can be functionalized by either catalytic doping or incorporation of nanovariants, is considered to be a potential promise for hydrogen storage. It was reported that polyaniline could store as much as 6–8 wt% of hydrogen [50], which, however, another team of scientists could not reproduce [51]. Yet another recent study reveals that a hydrogen uptake of 1.4–1.7 wt% H_2 has been reported for the polymers of intrinsic microscopy [52]. Polyaniline is a conductive polymer, with conductivity on the order of 10^0 S/cm. This is higher than that of typical nonconducting polymers, but much lower than that of metals [53]. In addition to its conductivity, polyaniline emeraldine base (EB) is very simple and inexpensive to polymerize. It is because of this simplicity that it was chosen as a matrix material for the nanocomposite structure.

Figure 8 represents the hydrogen sorption kinetics of polyaniline nanospheres at room temperature. From this figure, it is discernible that the hydrogen uptake and release of ~4.0 wt.% occurs in the initial run. However, during the consecutive cycles, the hydrogen storage capacity and kinetics were decreased. The SEM microstructure of polyaniline nanospheres are shown in Figure 9(a). Uniform cluster sizes of 50–100 nm are widely distributed over the surface. The microstructures after hydrogen sorption cycles exhibit microchannels or microcrack formation (see Figure 9(b)).

This correlates very well with effective hydrogenation as observed from sorption kinetic profiles (see Figure 8). Further cyclic reversibility and associated mechanistic behavior for hydrogen uptake and release kinetics are still underway.

Functionalization (see schematic Figure 10) has been carried out by the introduction of chemical groups into a polymer molecule or conversion of one chemical group to another group, which leads to a polymer with chemical, physical, or other functions. Functional polymers act as a catalyst to bind selectively to particular species, to capture and transport electric charge or energy, and to convert light into charge carriers and vice versa.

2.5. *High-surface area sorbents and new materials concepts*

There is a pressing need for the discovery and development of new reversible materials. One new area that may be promising is that of high-surface area hydrogen sorbents based on microporous metal-organic frameworks (MOFs). Such materials are synthetic, crystalline, and microporous and are composed of metal/oxide groups linked together by organic struts. Hydrogen storage capacity at 78 K (−195°C) has been reported as high as 4 wt% via an adsorptive mechanism, with a room temperature capacity of approximately 1 wt% [54]. However, due to the highly porous nature of these materials, volumetric capacity may still be a significant issue.

Another class of materials for hydrogen storage may be clathrates [15], which are primarily hydrogen-bonded H_2O frameworks. Initial studies have indicated that significant amounts of hydrogen molecules can be incorporated into the sII clathrate. Such materials may be particularly viable for off-board storage of hydrogen without the need for high pressure or liquid hydrogen tanks.

3. SUMMARY

Nanostructured materials such as nanotubes, nanofibers, and nanospheres show potential promise for hydrogen storage due to high-surface area, and they may offer several advantages for the physicochemical reactions, such as surface interactions, adsorption in addition to bulk absorption, rapid kinetics, low-temperature sorption, hydrogen atom dissociation, and molecular diffusion via the surface catalyst. The intrinsically large surface areas and unique adsorbing properties of nanophase materials can assist the dissociation of gaseous hydrogen, and the small volume of individual nanoparticles can produce short diffusion paths to the materials' interiors. The use of nanosized dopants enables a higher dispersion of the catalytically active species, and thus facilitates higher mass transfer reactions. Nanocomposites based on polymer matrix and functionalized carbon nanotubes possess unique microstructure for physisorption of hydrogen atom/molecule on the surface and inside the bulk. This review paper discussed briefly various nanomaterials for hydrogen storage and also presented hydrogen uptake and release characteristics for polyaniline nanospheres at room temperature.

ACKNOWLEDGMENTS

Financial support from US Department of Energy (Contract no. DE-FG36-04GO14224) and QuantumSphere Inc. is gratefully acknowledged. The authors also thank Dr. Rakesh Joshi for his comments and suggestions.

REFERENCES

[1] S. Satyapal, J. Petrovic, and G. Thomas, "Gassing up with hydrogen," *Scientific American*, vol. 296, no. 4, pp. 80–87, 2007.

[2] M. S. Dresselhaus and I. L. Thomas, "Alternative energy technologies," *Nature*, vol. 414, no. 6861, pp. 332–337, 2001.

[3] B. Sakintuna, F. Lamari-Darkrim, and M. Hirscher, "Metal hydride materials for solid hydrogen storage: a review," *International Journal of Hydrogen Energy*, vol. 32, no. 9, pp. 1121–1140, 2007.

[4] E. K. Stefanakos, D. Y. Goswami, S. S. Srinivasan, and J. T. Wolan, "Hydrogen energy," in *Environmentally Conscious Alternative Energy Production*, M. Kutz, Ed., vol. 4, chapter 7, pp. 165–206, John Wiley & Sons, New York, NY, USA, 2007.

[5] S. A. Sherif, F. Barbir, T. N. Veziroglu, M. Mahishi, and S. S. Srinivasan, "Hydrogen energy technologies," in *Handbook of Energy Efficiency and Renewable Energy*, F. Kreith and D. Y. Goswami, Eds., chapter 27, CRC Press, Boca Raton, Fla, USA, 2007.

[6] E. Fontes and E. Nilsson, "Modeling the fuel cell," *The Industrial Physicist*, vol. 7, no. 4, p. 14, 2001.

[7] R. H. Jones and G. J. Thomas, *Materials for the Hydrogen Economy*, CRC Press, Boca Raton, Fla, USA, 2007, Catalog no. 5024.

[8] Report of the Basic Energy Science Workshop on Hydrogen Production, Storage and use prepared by Argonne National Laboratory, May 2003.

[9] L. Schlapbach, "Hydrogen as a fuel and its storage for mobility and transport," *MRS Bulletin*, vol. 27, no. 9, pp. 675–676, 2002.

[10] C. Read, G. Thomas, C. Ordaz, and S. Satyapal, "U.S. Department of Energy's system targets for on-board vehicular hydrogen storage," *Material Matters*, vol. 2, no. 2, p. 3, 2007.

[11] A. Züttel, "Materials for hydrogen storage," *Materials Today*, vol. 6, no. 9, pp. 24–33, 2003.

[12] D. Chandra, J. J. Reilly, and R. Chellappa, "Metal hydrides for vehicular applications: the state of the art," *JOM*, vol. 58, no. 2, pp. 26–32, 2006.

[13] A. M. Seayad and D. M. Antonell, "Recent advances in hydrogen storage in metal-containing inorganic nanostructures and related materials," *Advanced Materials*, vol. 16, no. 9-10, pp. 765–777, 2004.

[14] F. E. Pinkerton and B. G. Wicke, "Bottling the hydrogen genie," *The Industrial Physicist*, vol. 10, no. 1, pp. 20–23, 2004.

[15] F. Schüth, "Technology: hydrogen and hydrates," *Nature*, vol. 434, no. 7034, pp. 712–713, 2005.

[16] F. Schüth, B. Bogdanović, and M. Felderhoff, "Light metal hydrides and complex hydrides for hydrogen storage," *Chemical Communications*, vol. 10, no. 20, pp. 2249–2258, 2004.

[17] N. B. McKeown, S. Makhseed, K. J. Msayib, L.-L. Ooi, M. Helliwell, and J. E. Warren, "A phthalocyanine clathrate of cubic symmetry containing interconnected solvent-filled voids of nanometer dimensions," *Angewandte Chemie International Edition*, vol. 44, no. 46, pp. 7546–7549, 2005.

[18] M. Fichtner, "Nanotechnological aspects in materials for hydrogen storage," *Advanced Engineering Materials*, vol. 7, no. 6, pp. 443–455, 2005.

[19] A. G. Wong-Foy, A. J. Matzger, and O. M. Yaghi, "Exceptional H_2 saturation uptake in microporous metal-organic frameworks," *Journal of the American Chemical Society*, vol. 128, no. 11, pp. 3494–3495, 2006.

[20] V. Renugopalakrishnan, A. M. Kannan, S. S. Srinivasan, et al., "Nanomaterials for energy conversion applications," *Journal of Nanoscience and Nanotechnology*. In press .

[21] E. G. Baburaj, F. H. Froes, V. Shutthanandan, and S. Thevuthasan, "Low cost synthesis of nanocrystalline titanium aluminides," Interfacial Chemistry and Engineering Annual Report, Pacific Northwest National Laboratory, Oak Ridge, Tenn, USA, 2000.

[22] R. Schulz, S. Boily, L. Zaluski, A. Zaluka, P. Tessier, and J. O. Ström-Olsen, "Nanocrystalline materials for hydrogen storage," Innovation in Metallic Materials, pp. 529–535, 1995.

[23] L. Schlapbach and A. Züttel, "Hydrogen-storage materials for mobile applications," *Nature*, vol. 414, no. 6861, pp. 353–358, 2001.

[24] W. Grochala and P. P. Edwards, "Thermal decomposition of the non-interstitial hydrides for the storage and production of hydrogen," *Chemical Reviews*, vol. 104, no. 3, pp. 1283–1316, 2004.

[25] B. Bogdanović and M. Schwickardi, "Ti-doped alkali metal aluminium hydrides as potential novel reversible hydrogen storage materials," *Journal of Alloys and Compounds*, vol. 253-254, pp. 1–9, 1997.

[26] C. M. Jensen and R. A. Zidan, "Hydrogen storage materials and method of making by dry homogenation," US patent 6471935, 2002.

[27] P. Chen, Z. Xiong, J. Luo, J. Lin, and K. L. Tan, "Interaction of hydrogen with metal nitrides and imides," *Nature*, vol. 420, no. 6913, pp. 302–304, 2002.

[28] Y. H. Hu and E. Ruckenstein, "H_2 storage in Li_3N. Temperature-programmed hydrogenation and dehydrogenation," *Industrial and Engineering Chemistry Research*, vol. 42, no. 21, pp. 5135–5139, 2003.

[29] J. J. Vajo, S. L. Skeith, and F. Mertens, "Reversible storage of hydrogen in destabilized $LiBH_4$," *Journal of Physical Chemistry B*, vol. 109, no. 9, pp. 3719–3722, 2005.

[30] M. Au, "Destabilized and catalyzed alkali metal borohydrides for hydrogen storage with good reversibility," US patent Appl. Publ 0194695 A1, 2006.

[31] S. S. Srinivasan, D. Escobar, M. Jurczyk, Y. Goswami, and E. K. Stefanakos, "Nanocatalyst doping of $Zn(BH_4)_2$ for on-board hydrogen storage," *Journal of Alloys and Compounds*, vol. 462, no. 1-2, pp. 294–302, 2008.

[32] J. Yang, A. Sudik, D. J. Siegel, et al., "Hydrogen storage properties of $2LiNH_2 + LiBH_4 + MgH_2$," *Journal of Alloys and Compounds*, vol. 446-447, pp. 345–349, 2007.

[33] G. J. Lewis, J. W. A. Sachtler, J. J. Low, et al., "High throughput screening of the ternary $LiNH_2$-MgH_2-$LiBH_4$ phase diagram," *Journal of Alloys and Compounds*, vol. 446-447, pp. 355–359, 2007.

[34] A. Züttel, "Hydrogen storage methods," *Naturwissenschaften*, vol. 91, no. 4, pp. 157–172, 2004.

[35] S. H. Joo, S. J. Choi, I. Oh, et al., "Ordered nanoporous arrays of carbon supporting high dispersions of platinum nanoparticles," *Nature*, vol. 412, no. 6843, pp. 169–172, 2001.

[36] A. Zaluska, L. Zaluski, and J. O. Ström-Olsen, "Structure, catalysis and atomic reactions on the nano-scale: a systematic approach to metal hydrides for hydrogen storage," *Applied Physics A*, vol. 72, no. 2, pp. 157–165, 2001.

[37] K.-J. Jeon, A. Theodore, C.-Y. Wu, and M. Cai, "Hydrogen absorption/desorption kinetics of magnesium nano-nickel composites synthesized by dry particle coating technique," *International Journal of Hydrogen Energy*, vol. 32, no. 12, pp. 1860–1868, 2007.

[38] X. Yao, C. Z. Wu, H. Wang, H. M. Cheng, and G. Q. Lu, "Effects of carbon nanotubes and metal catalysts on hydrogen storage in magnesium nanocomposites," *Journal of Nanoscience and Nanotechnology*, vol. 6, no. 2, pp. 494–498, 2006.

[39] C. Z. Wu, P. Wang, X. Yao, et al., "Hydrogen storage properties of MgH_2/SWNT composite prepared by ball milling," *Journal of Alloys and Compounds*, vol. 420, no. 1-2, pp. 278–282, 2006.

[40] S. R. Johnson, P. A. Anderson, P. P. Edwards, et al., "Chemical activation of MgH_2; a new route to superior hydrogen storage materials," *Chemical Communications*, no. 22, pp. 2823–2825, 2005.

[41] W. Luo, "($LiNH_2$-MgH_2): a viable hydrogen storage system," *Journal of Alloys and Compounds*, vol. 381, no. 1-2, pp. 284–287, 2004.

[42] J. Huot, G. Liang, S. Boily, A. Van Neste, and R. Schulz, "Structural study and hydrogen sorption kinetics of ball-milled magnesium hydride," *Journal of Alloys and Compounds*, vol. 293–295, pp. 495–500, 1999.

[43] P. Sudan, A. Züttel, Ph. Mauron, Ch. Emmenegger, P. Wenger, and L. Schlapbach, "Physisorption of hydrogen in single-walled carbon nanotubes," *carbon*, vol. 41, no. 2, pp. 2377–2383, 2003.

[44] B. Viswanathan, M. Sankaran, and M. A. Schibioh, "Carbon nanomaterials: are they appropriate candidates for hydrogen storage?" *Bulletin of the Catalysis Society of India*, vol. 2, pp. 12–32, 2003.

[45] M. G. Nijkamp, J. E. M. J. Raaymakers, A. J. van Dillen, and K. P. de Jong, "Hydrogen storage using physisorption—materials demands," *Applied Physics A*, vol. 72, no. 5, pp. 619–623, 2001.

[46] A. C. Dillon, K. M. Jones, T. A. Bekkedahl, C. H. Kiang, D. S. Bethune, and M. J. Heben, "Storage of hydrogen in single-walled carbon nanotubes," *Nature*, vol. 386, no. 6623, pp. 377–379, 1997.

[47] P. M. F. J. Costa, K. S. Coleman, and M. L. H. Green, "Influence of catalyst metal particles on the hydrogen sorption of single-walled carbon nanotube materials," *Nanotechnology*, vol. 16, no. 4, pp. 512–517, 2005.

[48] H. W. Kroto, J. R. Heath, S. C. O'Brien, R. F. Curl, and R. E. Smalley, "C_{60}: buckminsterfullerene," *Nature*, vol. 318, no. 6042, pp. 162–163, 1985.

[49] Y. Kojima and Y. Kawai, "IR characterizations of lithium imide and amide," *Journal of Alloys and Compounds*, vol. 395, no. 1-2, pp. 236–239, 2005.

[50] Y.-Y. Fan, A. Kaufmann, A. Mukasyan, and A. Varma, "Single- and multi-wall carbon nanotubes produced using the floating catalyst method: synthesis, purification and hydrogen uptake," *Carbon*, vol. 44, no. 11, pp. 2160–2170, 2006.

[51] S. J. Cho, K. S. Song, J. W. Kim, T. H. Kim, and K. Choo, "Hydrogen sorption in HCl-treated polyaniline and polypyrrole: new potential hydrogen storage media," *Fuel Chemistry Division Preprints*, vol. 47, no. 2, pp. 790–791, 2002.

[52] B. Panella, L. Kossykh, U. Dettlaff-Weglikowska, M. Hirscher, G. Zerbi, and S. Roth, "Volumetric measurement of hydrogen storage in HCl-treated polyaniline and polypyrrole," *Synthetic Metals*, vol. 151, no. 3, pp. 208–210, 2005.

[53] N. B. McKeown, B. Gahnem, K. J. Msayib, et al., "Towards polymer-based hydrogen storage materials: engineering ultramicroporous cavities within polymers of intrinsic microporosity," *Angewandte Chemie International Edition*, vol. 45, no. 11, pp. 1804–1807, 2006.

[54] J. L. C. Rowsell, E. C. Spencer, J. Eckert, J. A. K. Howard, and O. M. Yaghi, "Gas adsorption sites in a large-pore metal-organic framework," *Science*, vol. 309, no. 5739, pp. 1350–1354, 2005.